Analysis of the Activity Patterns in Focal Cortical Seizures using the 4-AP model

Thomais Asvestopoulou

Thesis submitted in partial fulfillment of the requirements for the

Masters' of Science degree in Computer Science and Engineering

University of Crete
School of Sciences and Engineering
Computer Science Department
Voutes University Campus, 700 13 Heraklion, Crete, Greece

Thesis Advisor: Prof. *Maria Papadopouli*

This work has been performed at the University of Crete, School of Sciences and Engineering, Computer Science Department.

This work has been supported by the Foundation for Research and Technology - Hellas (FORTH), Institute of Computer Science (ICS) and funded by the Hellenic Foundation for Research & Innovation for the support of postdoctoral researchers 2018-2021, on Dissecting Multi-Neuronal Modules of Computation in the Neocortex (neuronXnet) (PI: G. Tzagkarakis, Coordinator: M. Papadopouli), and by Fondation Santé, January 2019-2020 & 2020-2021 on Neuronal networks in epilepsy – Deciphering the role of activity patterns in focal cortical seizures (PI: M. Papadopouli)

University of Crete
Computer Science Department

Analysis of the Activity Patterns in Focal Cortical Seizures using the 4-AP model

Thesis submitted by
Thomais Asvestopoulou
in partial fulfillment of the requirements for the
Masters' of Science degree in Computer Science

THESIS APPROVAL

Author: _____
Thomais Asvestopoulou

Committee approvals: _____
Maria Papadopouli
Professor, Thesis Supervisor

_____
Stelios Smirnakis
Associate Professor (Harvard Medical School), Committee Member

_____
Ioannis Tsamardinos
Professor, Committee Member

Departmental approval: _____
Polyvios Pratikakis
Assistant Professor, Director of Graduate Studies

Heraklion, November 2020

Analysis of the Activity Patterns in Focal Cortical Seizures using the 4-AP model

Abstract

Epilepsy affects about 3% of the worldwide population. It is characterized by the repeated occurrence of highly synchronized and unprovoked bursts of neuronal activity, known as seizures. However, our understanding of how neurons interact to generate the abnormal network activity patterns that underlie ictogenesis is limited. It is important to understand what changes in the cortical circuit allow a highly-correlated firing state to emerge, evolve, and recur. To analyse the emergence and spread of focally initiated seizures, we used the 4-aminopyridine (4-AP) model, a well-established, reliable model of acute focal neocortical seizures. Using the calcium indicator GCaMP6s with *in vivo* two-photon cellular microscopy, we examined the activity profiles of individual neurons in layer 2/3 (L2/3) of the visual cortex during focal seizures induced by 4-AP injections in mice.

We identified significant activity epochs in this context using two methodologies: a novel methodology based on the identification of the noise intervals of the fluorescence signal of each neuron, and another one based on the Recurrence Quantification Analysis, a powerful tool based on the topological analysis of the phase space of the underlying dynamics. Their results are consistent in terms of the presence of significant activity epochs and their duration. These approaches enable the identification of the onset of events of significant activity, aiming to dissect the mechanisms of seizure initiation and recruitment of neurons within the field of view.

We also characterized the functional network connectivity using graph-theoretical metrics, such as normalized degree of connectivity, clustering coefficient, and weighted clustering coefficient. To capture the contribution and influence of a neuron to the connectivity of the network within a larger region, we introduced the affinity, a belief-propagation-based metric, that integrates the pairwise temporal correlation of the firing events of neurons in a sub-network. The analysis reveals the structure of the functional networks after the 4-AP injection, the significant increase of the temporal correlation of neurons, and the influence of neurons in the region close to the 4-AP injection. It comparatively examines the findings with other network architectures, including the functional network of the control (prior to the injection) as well as random graphs with well-defined structure.

Ανάλυση των μοτίβων δραστηριότητας στις εστιακές επιληπτικές κρίσεις χρησιμοποιώντας το 4-AP μοντέλο

Περίληψη

Η επιληψία επηρεάζει περίπου το 3% του παγκόσμιου πληθυσμού. Χαρακτηρίζεται από την επαναλαμβανόμενη εμφάνιση συγχρονισμένων ξεσπασμάτων της δραστηριότητας των νευρώνων, τις ευρέως γνωστές επιληπτικές κρίσεις. Ωστόσο, η κατανόησή μας για το πως οι νευρώνες αλληλλεπιδρούν για να παράγουν μη κανονική λειτουργία του δικτύου που οδηγεί στην επιλεπτογένεση είναι περιορισμένη. Είναι λοιπόν σημαντικό να καταλάβουμε ποιες αλλαγές στο δίκτυο του εγκεφάλου επιτρέπουν αυτήν την υψηλά συσχετιζόμενη δραστηριότητα πυροδοτήσεων να εμφανιστεί, να εξελιχθεί, και να επαναληφθεί. Για την μελέτη του σχηματισμού και της εξάπλωσης των εστιακών επιληπτικών κρίσεων, χρησιμοποιήθηκε το 4-AP μοντέλο, ένα αξιόπιστο μοντέλο οξείων εστιακών επιληπτικών κρίσεων του νεοφλοιού. Χρησιμοποιώντας δείκτη ασβεστίου GCaMP6s σε πειράματα μικροσκοπίας δύο φωτονίων, εξετάστηκε η δραστηριότητα των επιμέρους νευρώνων του επιπέδου 2/3 του οπτικού φλοιού κατά την διάρκεια εστιακών κρίσεων που προκλήθηκαν από την έγχυση διαλύματος4-AP στον εγκέφαλο ποντικών.

Χρησιμοποιήθηκαν δύο μεθοδολογίες για την ανίχνευση περιόδων σημαντικής δραστηριότητας: η μια βασιζόμενη στην αναγνώριση διαστημάτων θορύβου στα σήματα φθορισμού του κάθε νευρώνα, και η λεγόμενη Ανάλυση Ποσοτικής Επαναληψιμότητας (RQA),που αποτελεί ένα ισχυρό εργαλείο που βασιζεται σε τοπολογική ανάλυση του χώρου φάσεων των υποβόσκουσων δυναμικών για την επαλήθευση των αποτελεσμάτων. Και οι δύο μέθοδοι ανιχνεύουν την έναρξη περιόδων σημαντικής δραστηριότητας, αναδύοντας τους μηχανισμούς της έναρξης των επιληπτικών κρίσεων. Επίσης, χαρακτηρίστηκε η λειτουργική συνδεσιμότητα του δικτύου χρησιμοποιώντας γραφοθεωρητικές μετρικές, όπως ο κανονικοποιημένος βαθμός συνδεσιμότητας (normalized degree of connectivity), ο συντελεστής συσταδοποίησης (clustering coefficient), αλλά και το affinity , μια μετρική που ενσωματώνει την χρονική συσχέτιση των πυροδοτήσεων των νευρώνων σε ένα υποδίκτυο, για την αξιολόγηση της συνεισφοράς και της επιρροής των νευρώνων στην συνδεσιμότητα του δικτύου σε μια ευρύτερη περιοχή. Η ανάλυση της παρούσας εργασίας αποκαλύπτει την δομή των λειτουργικών δικτύων των νευρώνων μετά την τοπική έγχυση του 4-AP,την σημαντική αύξηση του χρονικού συσχετισμού των πυροδοτήσεων των νευρώνων, υπογραμμίζοντας την επιρροή τους σε μια περιοχή κοντά στο σημείο έγχυσης της ουσίας. Επίσης, συγκρίνει τα ευρήματα με άλλες δικτυακές αρχιτεκτονικές, συμπεριλαμβανομένου του λειτουργικού δικτύου κάτω από κανονικές συνθήκες (πριν την έγχυση ουσίας που προκαλεί τις κρίσεις), καθώς και με γράφους που έχουν σαφώς ορισμένη δομή/μορφή.

Ευχαριστίες

Με την ολοκλήρωση της μεταπτυχιακής μου εργασίας, θα ήθελα να εκφράσω τις θερμές μου ευχαριστίες σε όλους αυτούς που συνέβαλλαν στην εκπόνησή της.

Ευχαριστώ θερμά την επιβλέπουσα καθηγήτριά μου, κύρια Μαρία Παπαδοπούλη, για την εμπιστοσύνη που μου έδειξε εξ' αρχής, αναθέτοντάς μου το συγκεκριμένο θέμα, την επιστημονική της καθοδήγηση και τις υποδείξεις της, τη συνεχή της υποστήριξη, και το αμείωτο ενδιαφέρον που έδειξε από την αρχή μέχρι το τέλος. Επίσης, ευχαριστώ τον καθηγητή νευρολογίας, κύριο Στέλιο Σμυρνάκη, για τις εποικοδομητικές του υποδείξεις και την πολύτιμη συμβολή τους στην ολοκλήρωση αυτής της εργασίας παρέχοντας σημαντικές πληροφορίες και διαφωτίζοντας το βιολογικό κομμάτι των αποτελεσμάτων της παρούσας εργασίας. Ακόμη, πολύτιμη ήταν η συμβολή του Dr. Joseph Lombardo, μέλος του εργαστηρίου του κου. Σμυρνάκη, ο οποίος διενέργησε τις απαιτούμενες εργαστηριακές διαδικασίες και τις μετρήσεις, την αρχική προεπεξεργασία των δεδομένων, και παρείχε χρήσιμες πληροφορίες για αυτές τις διαδικασίες.

Επιπλέον, ιδιαίτερες ευχαριστίες θα ήθελα να απευθύνω στα μέλη του εργαστηρίου της κας. Παπαδοπούλη στο ΙΤΕ για τη συνεργασία, τη βοήθεια και την συμβολή τους στην εργασία, καθ' όλη τη διάρκεια της ερευνητικής διαδικασίας. Συγκεκριμένα θα ήθελα να ευχαριστήσω τη μεταδιδακτορική ερευνήτρια Δρ. Μαρία Μαρκάκη για την δουλειά της πάνω στην εργασία στα πλαίσια της διενέργειας της ανάλυσης του belief propagation και του affinity metric, αλλά και τον ερευνητή Δρ. Γιώργο Τζαγκαράκη για την διενέργεια της recurrence quantification analysis. Επίσης, σημαντική ήταν η συμβολή του Δρ. Ιωάννη Σμυρνάκη στην διαμόρφωση του τελικού pipeline του deconvolution.

Ακόμη, θα ήθελα να ευχαριστήσω την οικονομική υποστήριξη των φορέων χρηματοδότησης αυτής της ερευνητικής δραστηριότητας. Συγκεκριμένα, το Ελληνικό Ίδρυμα Έρευνας και Καινοτομίας (ΕΛΙΔΕΚ) μέσω του προγράμματος "Dissecting Multi-Neuronal Modules of Computation in the Neocortex / 2285 / neuronXnet" (επιστημονικά υπέυθυνος: Γιώργος Τζαγκαράκης, συντονίστρια: Μαρία Παπαδοπούλη), και τον οργανισμό Fondation Santé μέσω του προγράμματος "Neuronal Networks in Epilepsy-Deciphering the Role of Activity Patterns in focal Cortical Seizures"(επιστημονικα υπεύθυνη: Μαρία Παπαδοπούλη).

Τέλος, θα ήθελα εκφράσω την ευγνωμοσύνη μου στην οικογένειά μου και τους κοντινούς μου ανθρώπους για όλη την ψυχολογική και όχι μόνο υποστήριξη, τη συμπαράσταση και την κατανόησή τους, καθ' όλη τη διάρκεια των μεταπτυχιακών μου σπουδών και εκπόνησης της παρούσας εργασίας.

to my loved ones

Contents

List of Tables

List of Figures

List of Abbreviations

4-AP 4-aminopyridine.

DoC Degree of Connectivity.

ECoG Electrocorticogram.

EEG Electroencephalogram.

ER Erdös-Rényi.

FoV Field of View.

LOI line of identity.

LOS line of synchronization.

PSD Power Spectral Density.

ROI Region of Interest.

RP recurrence plot.

RQA Recurrent Quantification Analysis.

STTC Spike Time Tiling Coefficient.

WCC Weighted Clustering Coefficient.

WS Watts-Strogatz.

Chapter 1

Introduction

Epilepsy affects about 3% of the worldwide population. It is characterized by the repeated occurrence of highly synchronized and unprovoked bursts of neuronal activity, known as seizures [2]. Brain-injury patients carry high-risk of developing epilepsy for decades following the injury, causing morbidity [3]. Injury causing epilepsy typically leads to excitation/inhibition imbalance, which drives neural circuits into self-perpetuating oscillatory activity-states, feeding the hypersynchronous epileptic-bursts seen on cortical-surface EEG [4, 5]. Our knowledge of how exactly do neurons interact to generate the abnormal network activity patterns that underlie ictogenesis is limited [6]. It is important to understand what changes in the cortical circuit allow a highly-correlated firing state to emerge, evolve, and recur after focal-cortical injury.

The large number of people affected by epilepsy outlines the need for more extensive research for the diagnosis, treatment, and potential prevention of this neurogenerative disorder. Even though research on human epilepsy should be ideally based on human patients, various ethical constraints arise, such as the invasiveness of the applied methods and the difficulty to control the conditions under which measurements are conducted. For this reason animal models of epilepsy are vital to epilepsy research. Animal models of epilepsy are mostly used to elucidate the fundamental neuronal mechanisms of brain function (normal and epileptic) but also for research related to novel therapeutic interventions.

Several models of acute focal neocortical epilepsy have been established in the past. One of them is the 4-aminopyridine (4-AP) model, a well-established, reliable model of acute focal neocortical seizures [7, 8, 9, 10, 11, 12, 13], that has been used successfully in the past to test the potential of various therapeutic approaches [14, 15] [1]. It allows to control and standardize the extent of the focus,

[1] One possible criticism is that the team could have chosen a more realistic focal epilepsy model, such as epilepsy in a mouse model of traumatic brain injury [16, 17], stroke [18] or after hemoglobin or iron injection [19, 20]. These models are undeniably important and they do plan to study them in the future. However, in order to increase the power of our observations, it is important to begin our study in an established model where we can control as many variables as possible.

particularly as the 4-AP spread after temporally restricted application is limited [21]. Since the 4-AP primarily induces focal hyper-excitability, it provides a way to directly observe how the resulting excitation/inhibition imbalance emerges around the cortical focus and how it spreads in cortical circuits in the context of essentially normal inhibition [22]. This is a difficult task in direct injury models, in which there is not *a priori* knowledge of which regions in the highly variable penumbra of the lesion play the important role in epileptogenesis.

We study focal epileptic seizures at the visual cortex (V1) with simultaneous electrocorticography (ECoG) and two-photon imaging microscopy. The visual cortex was chosen as it allows us to take advantage of existing background knowledge and to directly measure how epileptic circuits respond to provocation by epileptogenic photic stimulation. Well-established methods can be used to measure cell gain and contrast response functions of different cell types [23], evaluating how these properties change in the epileptic state. Observing a deviation in these properties from normal will strongly suggest the mechanism that underlies cortical network malfunction. ECoG, a specific type of EEG, combines adequate temporal and spatial resolution with low risks of medical complications compared to other invasive methods. This is also a valuable tool as the onset of a seizure is often characterized by abrupt frequency changes in the EEG.

Objectives In the current thesis, we aim to unravel the neuronal activity patterns of focal epilepsy initiation and progression. We examine the finer spatio-temporal dynamics of the ictogenesis process, and micro-phases, including the order of the recruitment of neurons in the seizures. The analysis follows two directions: (a) the functional network connectivity characterisation under different states, using both weighted and unweighted graphs, and metrics, such as degree of connectivity, clustering coefficient, and belief propagation based activity, and (b) the detection of significant activity patterns of the fluorescence signals analysis under epileptic conditions. Fig. 1.1 presents a summary of this analysis.

Innovation To the best of our knowledge is the first study that discusses the functional network connectivity in the context of 4-AP induced seizures. It is also the first time Fast Belief Propagation is applied on neural data, and specifically on weighted graphs, revealing the neurons with the influence on the network during epileptic conditions. Towards the second direction we developed a novel method of identification of periods of significant fluorescence activity on neuron and population level but also employed Recurrence quantification Analysis (RQA), a powerful tool based on the topological analysis of the phase space of the underlying dynamics. Finally, we used ranking correlation metrics to assess the recruitment order of neurons across significant activity epochs and showed that recruitment mechanisms change over time, as the seizure-like activity contaminates the imaged region.

Contributions Parts of this work have been submitted acknowledged conferences. Our abstract titled "Using RQA to identify the structure of 4-AP induced seizure events" by T. Asvestopoulou, M. Kampourakis, M. Markaki, J. Lombardo, G. Palagina, S. Smirnakis, and M. Papadopouli, was submitted and accepted for presentation at AREADNE 2020 (Research in Encoding And Decoding of Neural

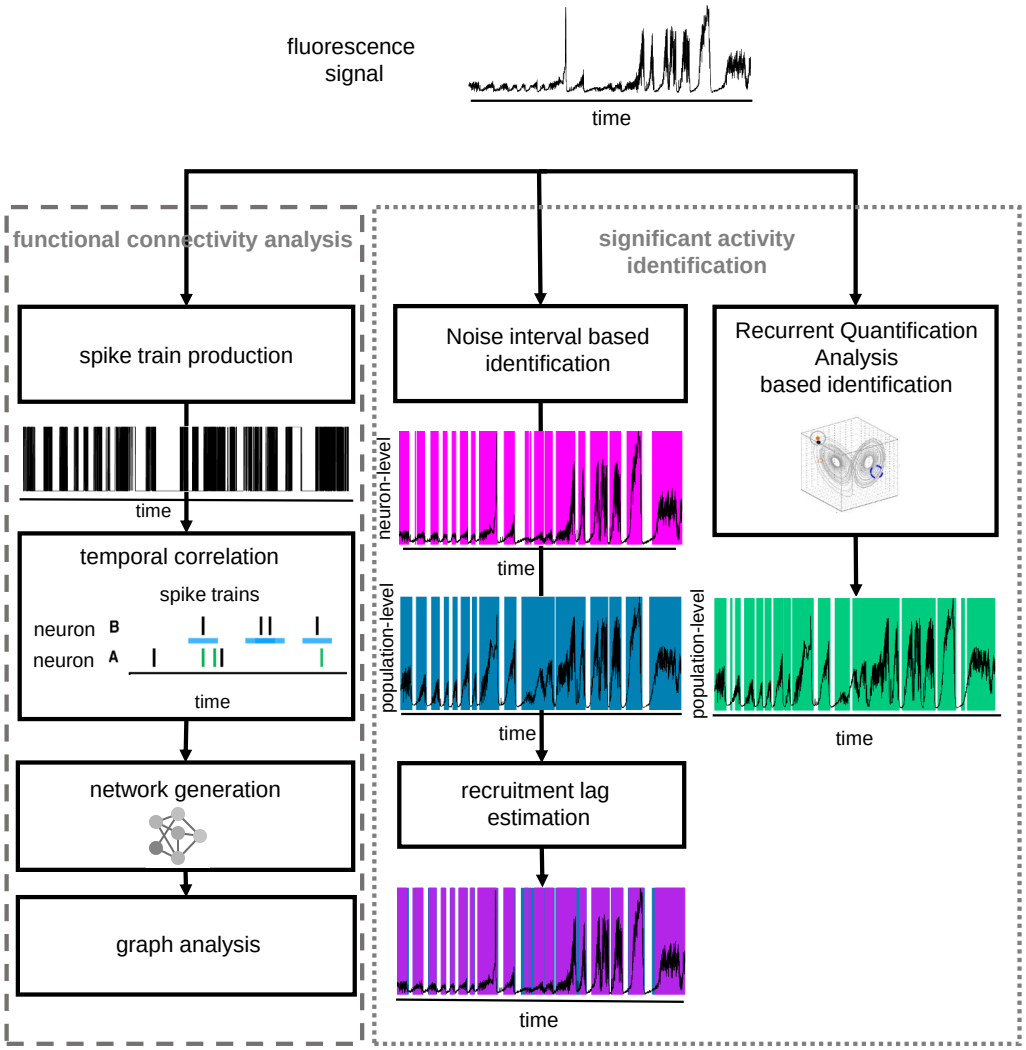

Figure 1.1: Overview of the main methodology. Two main threads: (a) Functional connectivity analysis through temporal correlation of the obtained spike trains, and (b) Identification of significant activity during epileptic seizures using two different approaches; a novel method based on the noise intervals identification, and Recurrent Quantification Analysis (RQA), a tool able to understand the underlying dynamics of a signal.

Ensembles) . Recently (late October 2020), two papers were also submitted for review at International Conference on Acoustics, Speech and Signal Processing

(ICASSP) 2021, namely "On Functional Network Connectivity in Focal Neocortical Seizures using Belief-Propagation Metrics" by T. Asvestopoulou, M. Markaki, J. Lombardo, S. M. Smirnakis, M. Papadopouli, and "On the Identification and Characterization of epochs of significant changes in Focal Neocortical Seizures" by T. Asvestopoulou, G. Tzagkarakis, J. Lombardo, S. M. Smirnakis and M. Papadopouli. By the completion of the validation process with the rest of the available datasets, we plan to publish our results in an acknowledged neuroscience journal.

The rest of the thesis is structured as follows: Section 2 does a literature review about epilepsy and its characteristics, recording of brain activity, the 4-AP model and recent related work. Section 3 presents the methods for the analysis described in Section 5. Finally, Section 6 summarizes of the key results and describes our future work plans.

Chapter 2

Related Work

This chapter provides an overview of the visual cortex and epilepsy in the brain, its etiology, and its main clinical characteristics. It also describes the two methods used for the activity monitoring. First, it describes the two-photon imaging, its advantages over one-photon imaging, and the main restrictions of the method. Then, it provides a description of the EEG and ECoG, methods used to record the electrical signals of the brain and how to study their spectral characteristics. It also describes some differences between the human and rodent frequencies in the brain. Finally, it provides a description of the 4-AP model and its characteristics, and an overview of the most recent 4-AP studies.

2.1 Brain & the primary visual cortex

The human brain is a complex structure. It contains about 100 billion neurons [24] connected with other neurons through synapses. The majority of these cells are found in the cerebellum and the neocortex. The cerebellum plays an important role in motor control, while the neocortex is involved in higher-order brain functions such as perception, cognition, generation of motor commands, and language [25].

Neocortex is a six-layered, folded, sheet-like structure that consists of billions of neurons, both excitatory and inhibitory. Inhibitory interneurons modulate the activity of excitatory pyramidal neurons which transmit information between neuronal assemblies. Appropriate brain function depends on highly interconnected and well-organized networks of the inhibitory interneurons and excitatory pyramidal neurons in a balanced excitation–inhibition interaction [26, 27, 28]. Imbalance between these network components can lead to brain malfunction and neurological diseases, including epilepsy, schizophrenia, and autism-spectrum disorder [29].

The neocortex is divided into regions named after the overlying cranial bones: the frontal, the parietal, the occipital, and the temporal lobes, which perform different functions. Visual information is passed from the retina to the lateral geniculate nucleus (LGN) and from there to the temporal lobe, that contains primary visual cortex (V1). V1, which also consists of six layers of cells, is the

primary relay of visual information to the rest of the cortex and serves as a model area for studying visual representations in the brain. It receives sensory inputs in layer 4 (L4), processed vertically through the cortical column and laterally within each layer, and then projected "forward" to higher areas by V1 layers 2/3 (L2/3), and "backwards" as feedback to lower areas by V1 layers 5/6 (L5/6) [30].

The study of the visual cortex allows to take advantage of existing background knowledge and to directly measure how circuits respond to provocation by epileptogenic stimulation. Well-established methods can be used to measure cell gain and contrast response functions of different cell types [23], evaluating how these properties change in the epileptic state. Observing a deviation in these properties from normal will strongly suggest the mechanism that underlies cortical network malfunction.

2.2 Epilepsy

Epilepsy is one of the most common neurological disorders affecting about 50 million people worldwide (according to the World Health Organization 2019 factsheet on epilepsy), characterized by the repeated occurrence of highly synchronized and unprovoked bursts of neuronal activity, known as seizures [2]. It is a diverse disorder with several recognized epileptic syndromes [31]. Focal seizures typically start in confined brain regions and remain restricted to these areas (simple focal seizures) or spread to other brain regions (secondary generalization). By contrast, generalized seizures are characterized by the synchronous bihemispheric onset of epileptic activity on EEG. The mechanisms leading to these different types of seizures and epileptic syndromes still need to be clarified [6]. However, recent genetic studies in patients with epilepsy, and the ongoing investigation of various animal models of epilepsy, shed light on epileptogenesis (the processes leading to epilepsy) and ictogenesis (the process of seizure initiation) mechanisms.

Patients with post-traumatic brain injury carry a high risk of epilepsy for decades following the injury, causing considerable morbidity [3]. Acquired trauma and other etiologies that cause epilepsy typically lead to imbalance between excitation and inhibition, which drives neural circuits into self-perpetuating oscillatory activity states, feeding hyper-synchronous epileptic bursts seen on ECoG [4, 5]. Understanding what local cortical control mechanisms can abort the transition from short, locally "contained", ictal events, to longer, larger ictal events that spread across cortical circuits including contralateral cortex is highly relevant to post-traumatic epilepsy. Cortical malfunction is common in epilepsy syndromes of traumatic origin [32, 33].

An important question in epilepsy is how single units get recruited *in vivo* during the evolution of seizure events. Specifically, it is not known whether neurons fire in a stereotyped pattern or sequence per seizure event, whether this happens reliably, and how it depends on cell type. It is important to determine whether

special ("gate") units exist that are reliably engaged, potentially orchestrating certain patterns, and may therefore play an important role in seizure generation or propagation. The identification of patterns of neuronal synchronicity (the so called "functional connectivity" [34]) helps to understand how the interaction between excitatory neurons and specific classes of inhibitory interneurons, as well as among sets of neurons forming distinct "sub-networks", leads to a transition from the normal (essentially uncorrelated) to the abnormal (highly correlated) cortical-circuit state, and how this period of hyper-synchrony starts, escalates, and finally ends. Studying epileptic models *in vivo* is important, since the full connectivity of epileptic circuits is preserved [35], but still at its infancy. Note that being "functionally connected" does not necessarily mean that neurons are anatomically connected to each other. We need to understand what changes in the cortical circuits allow correlated firing to emerge, evolve, and recur after focal cortical injury. Specifically, we need to understand what is the sequence of recruitment of individual neurons into epileptic events *in vivo*, how properties of recruitment change over time, how recruitment depends on the interaction between excitatory neurons and specific classes of inhibitory interneurons, and whether recruitment proceeds more efficiently along some circuit pathways more than others.

2.3 Two-photon imaging

The two-photon microscopy technique is a fluorescence imaging technique, first introduced by Denk *et al.* [36] that allows for imaging of living tissue. One major limitation of this method is the need of a fluorescent specimen. Towards this end, fluorescent calcium sensors have been developed. A known family of ultrasensitive protein calcium sensors (GCaMP6) is widely used, as it has been proved that in layer 2/3 pyramidal neurons of the mouse visual cortex *in vivo*, it can reliably detect single action potentials in neuronal somata [37]. It relies on the phenomenon of two-photon excited fluorescence. Two infrared photons must collide with a fluorophore (i.e., a fluorescent chemical compound that can re-emit light upon light excitation) simultaneously. Then, their combined energy excites the fluorophore. This excitation is similar to excitation caused by a single photon of about half the wavelength. The fluorophore relaxes back to the ground state, emitting a visible photon. Because a fluorophore must absorb two photons per excitation event, fluorescence depends on the square of the infrared light intensity. This non-linear effect, combined with the sharp focusing of a microscope objective lens, allows one to excite only a diffraction-limited spot within the specimen [38]. Compared to one-photon imaging, it provides several advantages: It dramatically reduces phototoxicity and dye bleaching, resulting to enhanced signal-to-noise ratio. It also makes possible to reach greater imaging depths [38].

2.4 Electrical signals in the brain and epilepsy

Our brain is the central control and processing unit. The neural activity of the brain uses action potentials by which the brain activity can be recorded by means of electrodes, such as in electroencephalogram (EEG). The analysis of the spectral properties of the EEG is an important aspect of understanding the signal. Specifically, the absence or presence of waves (and or spikes) in specific frequency bands is very useful for diagnostic purposes and the identification of several medical conditions.

The more typical frequency bands are the delta (δ), theta (θ), alpha (α), and beta (β) waves. Let us define them in more detail, from lower to higher frequencies.

Delta waves lie within the range 0.5 to 4 Hz and are associated with deep sleep. They can also be present in the waking state.

Theta band ranges from 4 to 7.5 Hz. These waves have been associated with access to unconscious material, creative inspiration and deep meditation. The name of this category is sometimes related to the physiological origin of these waves, the thalamus.

Alpha waves follow, ranging from 8 to 13 Hz. They appear in the posterior half of the head and are usually found over the occipital region of the brain and can be detected in all parts of brain posterior lobes. The alpha waves are the most prominent of the brain activity waves.

Beta waves lie within the range 13 to 26 Hz (however, in some references no upper bound is given). Beta waves are related to the waking state of the brain and associated with active thinking and paying attention, as well as problem solving, and is found in normal adults.

Frequencies above 30 Hz correspond to the gamma (γ) band. Even though these waves have very low amplitude and they rarely appear, detecting them can be used for confirmation of certain conditions of the brain.

In the literature these aforementioned frequency bands are more or less the same, but there may be some small variations of their limits. For example, Moffett *et al.* [39] also talked about expanding the "tranditional" frequency bands and introduced psi (ψ) band (260-280 Hz) and omega (ω) band that covers frequencies from 400 to 500 Hz. Also, Pizarro *et al.* [40] are using in their analysis a slightly different definition of the usual bands (delta (1 – 4 Hz), theta (4 – 8 Hz), alpha (8 – 13 Hz), beta (13 – 30 Hz)) and use some additional bands of lower (slow delta (0.1 – 1 Hz)) but also higher frequencies up to 500 Hz((gamma (30 – 70 Hz), high gamma (70 – 120Hz), ripples (120 – 250 Hz), and fast ripples (250–50 0Hz)).

As research evolves, differences between the human and rodent brain activity are revealed: Jing *et al.* [41] observed that rats have an overall faster frequency ($\sim$ 21 Hz posteriorly and 16 Hz anteriorly) than humans. Watrous *et al.* [42] mentioned that theta band in rodents (6-10 Hz) is different from human theta (4-7 Hz) and faster. Also, according to Maheshwari and Noebels [43] models of absence epilepsy in rodents are usually characterized by generalized spike-and-wave

discharges occurring at a rate from 5 to 9 Hz, which is much faster than the 3 Hz discharges of human patients with childhood absence epilepsy. High frequency bands (>80 Hz) analysis in rodent temporal lobe epilepsy models revealed that fast ripples (250-500 Hz) may be an indication of epilepsy, prior to the seizure activity (Lévesque and Avoli [44]).

Often the onset of a seizure is characterized by sudden frequency changes in the EEG. These changes lie usually within the alpha band (increase in amplitude during the seizure period). The transition from normal to ictal state for focal epileptic seizures constitutes of gradual changes and signal is transformed from chaotic to more ordered form. There is not a correlation of the EEG spikes to the severity of the seizure [45].

A special type of EEG is the electrocorticography (ECoG), which combines adequate temporal and spatial resolution with low risks of medical complications compared to other invasive methods. It is a neurophysiological technique used mostly in the operating room and records the same type of potentials as the scalp EEG. While ECoG resembles EEG recordings [46], it has greater amplitude (less attenuation of the signal as it is directly recorded from the brain surface), higher spatial resolution and broader frequency range [47]. ECoG is considered superior to EEG for monitoring cortical low-frequency oscillations [48] and high-frequency activity specifically in gamma range [47].

2.5 4-AP model of acute focal epilepsy

The 4-aminopyridine (4-AP) model is a well-established, reliable, model of acute focal neocortical seizures [7, 8, 9, 10, 11, 12, 13], that has been used successfully in the past to test the potential of various therapeutic approaches [14, 15]. It allows to control and standardize the extent of the focus (particularly as the 4-AP spread after temporally restricted application is limited [21]). Since 4-AP primarily induces focal hyper-excitability without immediate cell death or inflammation, it allows us to observe directly how the resulting excitation/inhibition imbalance emerges around the cortical focus and spreads in cortical circuits in the context of essentially normal inhibition. This is difficult to do in direct injury models, in which we do not know *a priori* which regions in the highly variable penumbra of the lesion play the important role in epileptogenesis.

More specifically, 4-aminopyridine (4-AP) is a specific blocker of transient potassium channels. It affects transient currents containing voltage-activated K^+ (Kv) 1.3 and 1.4 sub-units at low concentrations. 4-AP usually induces recurrent discharges in the rat hippocampus. Specifically, it elicits seizure-like events in parahippocampal structures [49] but also in the amygdala [50]. In interface recordings, the activity begins about 40 minutes after application of 50 or 100mM 4-AP [51].

2.6 4-AP model analysis related work

Over the last years several studies are focusing on 4-AP model of acute focal seizures and its properties. Rossi *et al.* [52] studied picrotoxin induced focal seizures in V1 of awake mice, and compared their propagation to the retinotopic organization of V1 and higher visual areas through simultaneous LFP recordings and wide-field imaging on transgenic mice expressing GCaMP in excitatory neurons. They categorised the epileptic-like activity of LFP measurements based on their shape and duration to seizures and interictal events. The events manifested different temporal and spectral features; The median reported seizure duration is 8.6 sec, while interictal events were much briefer with 0.5 sec median. Interictal events were characterized by a sharp decrease lasting 50-100 ms, opposed to seizures that were similar in terms of their onset, but were followed by rapid increase of activity and increased power in the range between 6 and 30 Hz. The majority of the events started in V1, close to injection site. Seizures propagated both locally but also to more distant homotopic (i.e., with matching retinotopic preference) areas, and eventually contaminated the entire visual cortex. Therefore, the seizure invasion does not only depend linearly on the cortical distance from the focus but also on homotopy (distance in visual preference). They try to approximate the spread in V1 with a gaussian function using the distace from the focus.

Wenzel *et al.* [53] combined local field potential (LFP) and two-photon imaging to investigate at single-cell level the spread of locally induced (4-AP or picrotoxin) seizures in anesthetized and awake mice. Most experiments in this study involved imaging of somatosensory cortex (layer 2/3). However, they also performed experiments where they imaged in visual cortex with consistent results. They were able to record the activity of different cortical layers and reported a reliable recruitment of local neural populations within and across cortical layers, along with the layer-specific temporal delays. Ictal events of layer 2/3 after the 4-AP injection involved continuous firing of a lot of neurons in a wave-fashion that slowly propagated across the FoV, opposed to the sparse firing in the absence of any injection and epileptic-like activity. Their analyses showed relatively stable recruitment ordering to subsequent seizures implying that seizures propagate in a spatially organized manner. However, the absolute ictal network recruitment ordering varied a lot in time. There is temporal variability across events, revealing an ictal network that stretches and compresses in time. Specifically, 4-AP induced seizures lasted 71 $\pm$ 7.1 sec.

In a follow-up study [54] they emphasized on 4-AP induced seizures in two spatially separated areas: the so-called initiation area (area of chemoconvulsant injection) and the propagation area (1.5-2 mm farther away). They reported that seizures originate within the initiation site and spread into farther away regions in a saltatory fashion. They demonstrated differences in the propagation patterns of seizures within the different areas. Specifically, within the propagation area seizure invasion occurs in a continuous wave of neuronal firing advancing slowly

across the FoV, while in the initiation site the invasion resembles a step-wise function. Moreover, they show a conserved spatial patterns of relative cell recruitment across seizures by ordering cell points based on time of recruitment (from early to late) and combined this information with the location of the cells. However, their patterns refer to a somehow crude clustering of neurons to 4 temporal quartiles. They also studied the interneurons' activity and found that they were among the neurons displaying the strongest calcium activity during the 40-second time period prior to the electrographic seizure onset. Also, interneurons manifest spatially heterogeneous recruitment patterns within epileptic networks. On average they increase their firing during ictal transition.

In a more recent study, Aeed *et al.* [55] used the 4-AP model of epilepsy with 2-photon calcium imaging and extracellular electrophysiological recordings on different types of neurons and different layers. They characterized epileptic-like discharges in the LFP in two categories: spikes (discharges with duration less than 0.5 seconds) and seizures (duration of at least 5 seconds). After the identification of these discharges they performed analysis on small windows around the onset in the Δf/f of individual neurons and examined the pairwise Pearson correlation of neurons' signals in these small windows around the (seizure/spike) onset. They report that the identified seizures lasted 74.4 $\pm$ 5.5 seconds and involved all the imaged cortical layers. Almost all the recorded seizures were accompanied by hyper-synchronous ictal onset patterns, with rhythmic high amplitude delta frequency components. They observed that both spikes and seizures involved rapid and synchronized activation of the recorded pyramidal neurons of layer 2/3. Moreover, these events were accompanied by recruitment of almost all the recorded PV-expressing interneurons. They hypothesize that PV-expressing interneurons fail to fully respond to the organized and intense activation of pyramidal neurons, leading to imbalance of excitatory to inhibitory activity in the cortex, which is what leads to seizures. Layer 4 neurons are synchronously recruited during the onset of events (in a similar way with layer 2/3). However, this layer does not develop transient excitatory to inhibitory imbalance at the onset of seizures. Opposing to layer 2/3, layer 5 pyramidal neurons were gradually and asynchronously recruited into seizures. They also used picrotoxin induced seizures (a different chemoconvulsant). Similar to 4-AP results, layer 2/3 initiated the epileptiform discharges and these only partially spread and reached layer 5 pyramidal cells.

Chapter 3

Background

This chapter provides the required background knowledge to understand the analysis of the next chapter. At first, the basics of the graph theory are described, which will make easier the understanding of the functional connectivity analysis. Then, we provide the basics of the spectral analysis that will be used to study the frequency components of the ECoG signals. A short description of the Spearman's rank coefficient follows, as it is used to assess whether the order of neurons' recruitment persists across recognized events. Then, two different variations of the Spike Time Tiling Coefficient, a measure that quantifies the temporal correlation of spike trains, are described. Finally, Recurrent Quantification Analysis, a tool based on the topological analysis of the phase space of the underlying dynamics of signals.

3.1 Graph Theory

Geometrically, a graph is defined as a set of points (vertices) in space connected with each other by a set of lines (edges). Mathematically, a graph $G = (V, E)$ consists of a set of nodes V and a set of edges E. An edge is specified by the vertices (or nodes) that it connects. If e is between v_i and v_j then $e_{ij} = (v_i, v_j)$ or $e_{ji} = (v_j, v_i)$. If a vertex v is connected with another vertex through an edge e, then we say that e is incident with v. Also if u and v are vertices connected to each other (there is an edge between them), then u is considered adjacent to v.

The degree of a vertex v, denoted by $d(v)$ is the number of edges that include vertex v. A path from v_1 to v_i, is a sequence edges that connect these two vertices. If v_1=v_i, then a cycle path exists in the graph. In a simple graph a path can be simply described by the sequence of vertices. If a vertex exists only once in a path , then the followed sequence is called a simple path. If each vertex appears once, then the path is called simple circuit. The length of a path is the number of edges it contains.

Two vertices v_i and v_j are connected if there is an edge from v_i to v_j. The vertex set of a graph can be divided to subsets of vertices V_1, V_2,..., V_k based on the

connections between vertices. A pair of vertices is connected if and only if they belong to the same subset of the vertex set partition. The sub-graphs induced in turn by the subsets V_1, V_2,..., V_k are called the components of the graph. A connected graph has only one component, otherwise it is disconnected.

In some applications we may need to provide a direction to each edge, which is presented with an arrow when we draw the graph. A graph with directed edges is called a directed graph or a digraph. If e is an edge of a digraph then the order of v_i and v_j becomes significant. The edge is be directed from the first vertex v_i to the second vertex v_j. Thus, if a digraph contains the edge (v_i, v_j) then it may or it may not contain the edge (v_j, v_i). For a vertex v, the out-degree $d^+(v)$ and the in-degree $d^-(v)$ are the number of edges starting from v and the number of edges ending up to v, respectively. A symmetric directed graph is a digraph in which for every edge (v_i, v_j) there is an edge (v_j, v_i). We call a digraph balanced if $d^+(v) = d^-(v)$ for every vertex v. Additional to the directed graphs, weighted graphs are very useful in some applications. To create a weighted graph a number (weight) $w(e)$ is assigned to each edge. [56]

Clustering coefficient is a measure of the degree to which nodes in a graph tend to group (cluster) together. This metric comes in two variations: the global and the local clustering coefficient. The global was designed to characterise the clustering of the entire graph, whereas the local refers to the connectivity of individual nodes of the graph.

A. Global clustering coefficient The global clustering coefficient is based on node triplets, i.e. three connected nodes. Three closed triplets, one centered on each of the nodes, create triangles. The global clustering coefficient is the number of closed triplets over the total number of all possible triplets. This can be applied to both undirected and directed networks and measures the clustering of the whole graph (global).

B. Local clustering coefficient As described earlier, a graph $G = (V, E)$ consists of a set of vertices V and a set of edges E that connect them. A vertex v_i is connected through edge e_{ij} with vertex v_j. The immediately connected neighbors of a vertex v_i constitute a neighborhood N_i :

$$N_i = \{v_j : e_{ij} \in E \quad \text{or} \quad e_{ji} \in E\}. \tag{3.1}$$

We define $k_i = |N_i|$ as the number of vertices in the neighbourhood, N_i. The local clustering coefficient C_i of a vertex v_i is defined as the proportion of connections between the immediately connected neighbors divided by the number of all the available connections that could exist between them. For a directed graph, for each neighborhood there are $k_i(k_i - 1)$ possible pairwise connections between the vertices. Thus, the local clustering coefficient for directed graphs is given as

$$C_i = \frac{|\{e_{jk} : v_j, v_k \in N_i, e_{jk} \in E\}|}{k_i(k_i - 1)}. \tag{3.2}$$

For an undirected graph $\frac{k_i(k_i-1)}{2}$ edges could exist between the vertices of a neighborhood. Thus, the local clustering coefficient for undirected graphs can be defined as

$$C_i = \frac{2|\{e_{jk} : v_j, v_k \in N_i, e_{jk} \in E\}|}{k_i(k_i-1)}. \tag{3.3}$$

The clustering coefficient ranges from 0 (if there is not any connection between the neighbors) to 1 (if all the neighbors are connected to each other within the neighborhood).

Affinity metric The Belief-Propagation (BP), an efficient inference algorithm on probabilistic graphical models, has been successfully applied to numerous domains, including error-correcting codes, stereo imaging in computer vision, fraud detection, and malware detection ([57] and references therein). It uses the principle of "homophily", i.e., the general assumption that neighbors influence each other. Indirectly, the affinity enables us to cluster the nodes in an unsupervised manner, by identifying their membership in a class/subnetwork.

To measure node affinity, i.e. influence of node i to node j, we calculate the affinity matrix S [57].

$$\mathbf{S} = [s_{ij}] = [\mathbf{I} + \epsilon^2\mathbf{D} - \epsilon\mathbf{A}]^{-1} \tag{3.4}$$

where:
s_{ij}: the affinity of node j w.r.t. node i.
I: $n \times n$ identity matrix,
A: $n \times n$ adjacency matrix with elements a_{ij},
D: $n \times n$ diagonal degree matrix, $d_{ii} = \sum_j a_{ij}$
ϵ: $1/(1+max_i(d_{ii}))$ positive constant (< 1) encoding the influence between neighbors.

The s_{ij} entry of the matrix indicates the influence node i has on node j and depends on all the r-step paths that connect nodes i and j. Intuitively, node i has more influence/affinity to node j if there are many, short, heavily weighted paths from node i to j.

Graph models with known properties

Erdös-Rényi (ER) model [58] is one of the first model networks and corresponds to a random graph. This random graph model is characterized by the number of vertices and the probability of edge existence between two randomly selected vertices. Each of the vertices pairs get connected with the same probability independently from other pairs. The Erdös-Rényi model became acceptable because its properties ease the network modeling.

Watts-Strogatz (WS) is also a random graph model. These graphs do have the small-world property, i.e. small average shortest path length and high clustering coefficient. Watts and Strogatz [59] created this category of graphs using interpolation of regular lattice with high clustering coefficient and random graph with

the small-world property. These graphs start from a ring lattice with each vertex having a degree k and with probability p to relocate. In this way, small values of p are sufficient to significantly reduce the shortest path length, while the clustering coefficient remains high. A graph has a small-world property when it has a high clustering coefficient and a small characteristic path length. High clustering coefficient values typically result in a high number of cliques and near-cliques, in other words they create sub-networks consisting of edges between all or almost all vertices. Small characteristic path length corresponds to easily reached vertices [60]. If L is the path length then it is considered small if $L \propto \log N$, where N is the number of vertices of the graph.

3.2 Spectral Analysis

The analysis of a signal is a fundamental problem of engineering and is essentially the process by which we obtain a better understanding of it and its characteristics. Examining the behaviour of a signal as time passes is one way of looking at a signal, known as time domain analysis. However, in many applications there are advantages in studying the behaviour of a signal with respect to frequency rather than time. This is known as frequency domain analysis. A frequency domain representation of a signal can take several forms, ranging from simple plots of amplitude or phase against frequency to more complex representations, such as modal response diagrams.

It is easy to convert a signal from time to the frequency domain with a pair of operators called transforms. The French mathematician Fourier introduced the so-called Fourier transform (FT), which is based on the assumption that any periodic waveform is equivalent to the sum of a number of sinusoids. By selecting the right amplitudes, frequencies and phases any periodic waveform may be synthesized. Each sinusoid used symbolizes a frequency component of the initial signal.

For a given signal $x(t)$ the Fourier transform is a useful tool in order to study its properties in the frequency domain. It is is calculated with the following formula (assuming that the signal $x(t)$ is continuous in time, i.e., ranging from $-\infty$ to ∞):

$$X(f) = \int_{-\infty}^{\infty} x(t) e^{-j2\pi ft}\, dt \tag{3.5}$$

$X(f)$ contains the values of this Fourier transformation and is also called the voltage density spectrum (in case of an electrical signal, such as the ECoG). Its units then will be Volts $\times$ sec.

Sometimes the description of a process through the FT is possible. This is why we use another metric of the frequency domain, the power spectral density (PSD).

First, we need to calculate the power P_{XX} of the signal $x(t)$:

$$P_{XX} = \lim_{T\to\infty} \frac{1}{2T} \int_{-T}^{T} E[X^2(t)]\, dt = \int_{-\infty}^{\infty} \lim_{T\to\infty} \frac{E[X_T(f)^2]}{2T}\, df \tag{3.6}$$

The power spectral density (PSD) can be defined as:

$$S_{XX}(f) = \lim_{T\to\infty} \frac{E[X_T(f)^2]}{2T} \tag{3.7}$$

$S_{XX}(f)$ has units of $\frac{Watt}{Hz}$ as this quantity multiplied with df in equation 3.2 (measured in Hz, as it represents frequency) will give us Watts, which is the unit of the estimated power P_{XX}. Based on that, the mean power of the signal can be estimated by the integral:

$$P_{XX} = \int_{-\infty}^{\infty} S_{XX}(f)\, df \tag{3.8}$$

From this we understand that the power spectral density describes the distribution of the signal's power in frequency domain.

This is the straight-forward way to calculate the PSD of a signal. However, we can calculate it using an intermediate step: by taking the FT of the auto-correlation of the signal.

All the above were based on the assumption of a signal recorded continuously in the history of time. In real life we usually have to estimate the PSD of a signal through a finite number of samples. This sets limitations to the quality of estimation of the PSD.

When a signal is statistically stable, the larger the sample size, the better the achieved estimation. But if the signal is not stable, it is not easy to select how big the sample needs to be to obtain a good estimation of its PSD. The quality of the estimation depends on how fast the variations of a signal are. So the target is to choose as less samples as possible that allow us to make a good estimation of the spectral.

Estimation power spectral of random signals: The periodogram
Signals of finite energy do have a FT and can be characterized in the frequency domain with use of their energy spectral density. On the contrary, signals of random processes do not have finite energy and therefore do not have FT. Such signals, do have finite mean power and therefore can be characterized from their PSD. [61] The real value of the PSD is the value of S_{XX} when T $\to \infty$ (equation 3.2). When finite number of samples are available to estimate the mean value by summing from 0 to $N-1$ lead to the transformed formula:

$$\frac{1}{N}|\sum_{n=0}^{N-1} x(n)e^{-j2\pi fn}| = \frac{1}{N}|X(f)|^2 \tag{3.9}$$

with $X(f)$ the FT of $x(n)$, which results from sampling from the $x(t)$. This form of estimation of spectral density is called *periodogram*.

Several methods have been proposed for the estimation of the periodogram, but Bartlett's [62] and Welch's [63] are the more commonly used. Both methods

do not make any assumptions about the signal and for this reason they are called non-parametric methods of PSD estimation. The Bartlett method aims to achieve variance reduction of the estimated periodogram. It splits the signal into non-overlapping windows of equal size, and then calculates the periodogram for each of these windows. The average of the windows' periodograms is the PSD estimate. The Welch method modifies the Bartlett method in two ways. It allows overlapping windows of the same size and applies a window function on the samples of each window.

Factors affecting PSD estimation. In case of using the periodogram itself (which considers the entire signal as one window, with use of rectangular windowing function) the number of points used for the FT calculation (DFT points N) determines the frequency resolution (i.e., how many Hz each DFT bin represents) of the spectrum based on the sampling frequency ($freq\ resolution = F_s/N$). A usually followed convention is to set N equal to the power of two that is next above the length of the signal. It is recommended not to set this parameter smaller than the signal length because the FT will only utilize the first N samples of the data to estimate PSD and eliminate the rest. In case of using windowing methods we have to be aware of the window function and length, the percentage of window overlapping, and the number of DFT points. Smaller window sizes increase the total number of windows the signal will be split into which results in turn to smooth PSD estimates because the random effects of noise will be averaged out. However, too small windows are compromising the frequency resolution. By increasing the overlapping of consecutive windows (for a given window size), the total number of windows to be considered is increased, which averages noise out. As for the number of DFT points it is recommended to be set equal to the window length.

3.3 Spearman's rank correlation

Spearman's rank test is a non-parametric method (not making any assumption about the underlying distribution of the data that are tested) that is used to measure the correlation of two variables X and Y. Instead of using the exact values of the variables, the data are ranked (i.e., ordered according to their values) from 1 to N, where N corresponds to the number of elements the variables. If X and Y are ranked in such a manner, the Spearman's rank correlation coefficient, is given by

$$r_S = 1 - \frac{6 \sum D^2}{N(N^2 - 1)} \tag{3.10}$$

where D denotes the differences between the ranks of corresponding values of X and Y, and where N is the number of pairs of values (X, Y) in the data.

It provides a measure of linear association between the ranks of the variables and its values range from -1 to 1. If r_S is fairly large and positive, then there is positive agreement between the ranks of the two variables. If r_S is close to -1, then,

when one variable has a high rank, the other one tends to have a low rank, and vice versa. Also, when r_S is near zero, the ranks of the two variables are almost independent [64].

3.4 Spike time tiling coefficient (STTC)

Towards the estimation of the temporal correlation among time-series of the firing events of neurons we need to be careful to take into consideration of the special features of spike trains. For relatively long time-series, Spike Time Tiling Coefficient (STTC) [1] is superior to commonly used measures, including Pearson, as it accounts for relative time shifts, local fluctuations of neural activity or noise, and the presence of periods without firing events. We also developed an advanced version of STTC that can integrate order (directionality).

To quantify the degree of correlation between firing events of two neurons A and B we used a modified version of the spike time tiling coefficient (STTC) [1] which was originally defined as:

$$\mathrm{STTC}_{A,B} = \frac{1}{2}\left(\frac{\mathrm{P}_A - \mathrm{T}_B}{1 - \mathrm{P}_A\mathrm{T}_B} + \frac{\mathrm{P}_B - \mathrm{T}_A}{1 - \mathrm{P}_B\mathrm{T}_A}\right) \tag{3.11}$$

where T_{A} the proportion of the recording duration within an interval Δt around each firing event of neuron A, P_{A} the proportion of firing events of neuron A found within an interval Δt around each firing event of neuron B, and likewise for T_{B} and P_{B}. This correlation index is robust against varying firing rates and has only one free parameter, the time window Δt.

To incorporate the temporal order of the firing events of two neurons A and B, we developed the directional STTC:

$$\mathrm{STTC}_{A,B} = \frac{1}{2}\left(\frac{\mathrm{P}_A^{B^-} - \mathrm{T}_{B^-}}{1 - \mathrm{P}_A^{B^-}\mathrm{T}_{B^-}} + \frac{\mathrm{P}_B^{A^+} - \mathrm{T}_{A^+}}{1 - \mathrm{P}_B^{A^+}\mathrm{T}_{A^+}}\right) \tag{3.12}$$

where T_{A^+} is the fraction of the total recording duration within a time window Δt after each spike of A T_{B^-} is the fraction of the total recording duration within a time window Δt before each spike of B, $P_{\mathrm{A}}{}^{\mathrm{B}^-}$ is the proportion of firing events of A within a time window Δt before each firing of B, and $P_{\mathrm{A}^+}{}^{\mathrm{B}}$ is the proportion of firing events of B within a time window Δt after each firing event of A. The directional STTC retains the desirable properties of the original STTC, while providing information on the temporal direction of correlation between two neurons. The directional STTC that excludes the synchronous spikes is called strictly directional STTC.

We chose to evaluate the STTC between neurons in our datasets with two different values for Δt based on physiological considerations: 0, 0.208 seconds. Specifically, we consider the *synchronous* firing of spike trains, as well as the strictly

directional firing with lag of one frame (0.208 seconds). In the first case the extent of synchronicity of neuronal firing is examined, while in the case of the strictly directional STTC we aim to study the diffusion of spikes in the neurons of the FoV.

To evaluate the extend to which the observed STTC values could arise by sequences with the same number of firing events without any temporal structure, we circularly shifted the firing events of each neuron A by a uniformly sampled integer number of imaging frames within the interval [1,$nframes$] 500 times independently, where $nframes$ is the total number of imaging frames. From these 500 iterations we obtained a *null* distribution of STTC values for each pair of neurons. The $z-score$ of each edge between neurons A and B is defined as

$$z_{A,B} = \frac{\mathrm{STTC}^{\mathrm{obs}}_{A,B} - \overline{\mathrm{STTC}^{\mathrm{null}}_{A,B}}}{\sigma^{\mathrm{null}}_{A,B}} \tag{3.13}$$

The $z-score$ quantifies the distance of the observed STTC value, $STTC^{obs}_{A,B}$, from the mean of the *null* STTC distribution, $\overline{\mathrm{STTC}^{\mathrm{null}}_{A,B}}$ which should be close to 0, in units of standard deviations of the *null* STTC distribution, $\sigma^{\mathrm{null}}_{A,B}$. High $z-score$ values correspond to statistically significant observed STTC values, i.e. temporal relationship that happens above chance.

3.5 Recurrent Quantification Analysis (RQA)

First, we give a brief overview of the global recurrence plot (RP), which is a key component of our proposed data analysis pipeline. More specifically, a RP is a square matrix whose elements express the times at which a state of a dynamical system recurs, thus revealing all the times when the *phase space trajectory* of the dynamical system visits roughly the same area in the phase space. To this end, RPs enable the investigation of an m-dimensional phase space trajectory through a two-dimensional representation of its recurrences. Such recurrence of a state occurring at time i, at a different time j is represented within a two-dimensional square matrix with ones (recurrence) and zeros (non-recurrence), where both axes are time axes.

Global recurrence plot (RP) of signal s. Given a signal s of length N, $\{r_i\}_{i=1}^{N}$, a phase space trajectory is reconstructed via time-delay embedding,

$$\mathbf{x}_i = [r_i,\, r_{i+\tau}, \ldots, r_{i+(m-1)\tau}] \;, \quad i = 1, \ldots, N_s \tag{3.14}$$

where m is the embedding dimension, τ is the delay, and $N_s = N - (m-1)\tau$ is the number of states. Having constructed a phase space representation, the RP is defined by

$$\mathbf{R}_{i,j} = \Theta\left(\varepsilon - |\mathbf{x}_i - \mathbf{x}_j|_p\right) \;, \quad i,\, j = 1, \ldots, N_s \;, \tag{3.15}$$

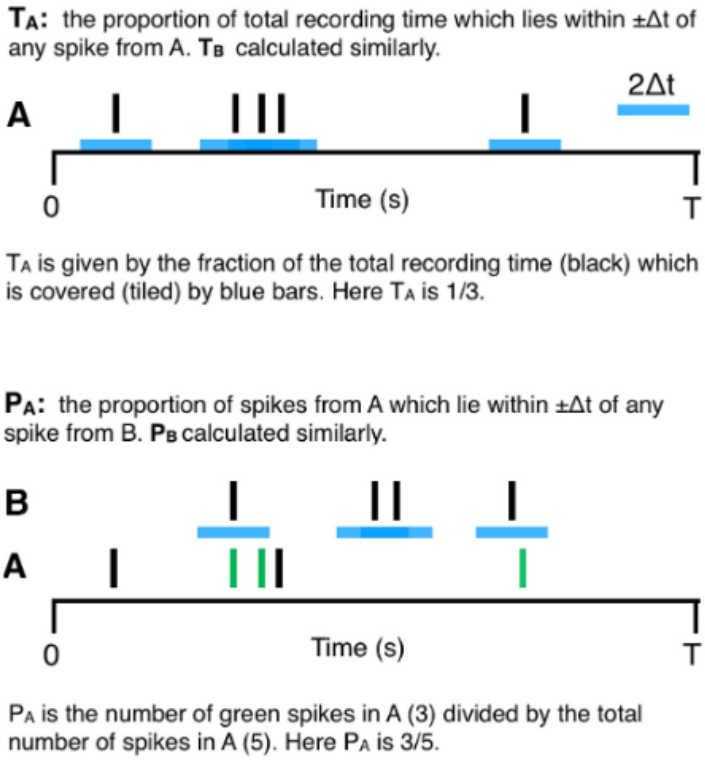

Figure 3.1: Diagram to demonstrate the calculation of the spike time tiling coefficient. The four quantities required to calculate the spike time tiling coefficient are P_{A}, P_{B}, T_{A}, T_{B}. The only free parameter is Δt. Values and scales are for demonstration only. Plot adopted from Cutts *et al.* [1].

where $\mathbf{x}_i, \mathbf{x}_j \in \mathbb{R}^{\,m}$ are the states, ε is threshold, $|\cdot|_p$ denotes a general ℓ_{p} norm (Euclidean distance ($p = 2$) is commonly used), and $\Theta(\cdot)$ is the Heaviside step function, whose discrete form is defined by

$$\Theta(n) = \begin{cases} 1, & \text{if } n \geq 0 \\ 0, & \text{if } n < 0 \end{cases}, \quad n \in \mathbb{R}\ . \tag{3.16}$$

The resulting matrix $\mathbf{R}$ exhibits always a main diagonal, $\mathbf{R}_{i,i} = 1$, $i = 1, \ldots, N$, also known as the *line of identity* (LOI). Typically, several linear (and/or curvilinear) structures appear in RPs, which give hints about the time evolution of the high-dimensional phase space trajectories. Besides, a major advantage of RPs is that they can also be applied to rather *short* and even *non-stationary* data. Since we are interested in detecting precisely the onset and offset times of events in the associated sequence $\mathbf{t}$, a global RP can enhance the understanding of the phase space trajectories and detect *phase synchronous* dynamics even when two distinct states of $\mathbf{r}$ do not converge.

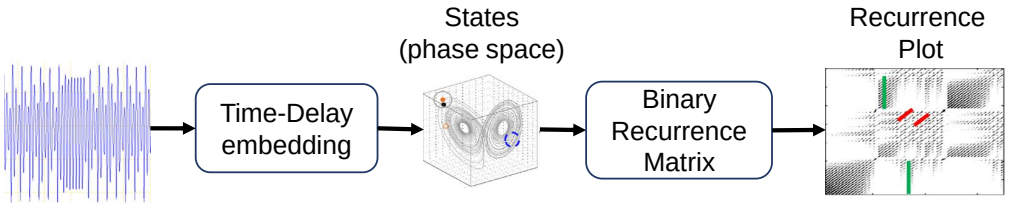

Figure 3.2: Recurrent Quantification Analysis pipeline for the detection of state changes (or events) in a signal.

Estimation of embedding parameters. In our implementation, the optimal time delay τ is estimated as the first minimum of the average mutual information (AMI) function [65]. Concerning the embedding dimension m, a minimal sufficient value is estimated using the method of false nearest neighbours (FNN) [66]. In practice, the minimal embedding dimension is defined as the dimension for which the fraction of false neighboring points is zero, or at least sufficiently small.

State-change onset/offset detection method. A key property of RPs, which is exploited in the detection of state-change instants, is that it reveals the local difference of the dynamical evolution of close trajectory segments in the phase space of the signal s. A time dilation or a compression of the time intervals, where a state-change appears in the signal, causes a distortion of the diagonal lines in the corresponding RP. Then, the LOI will be disrupted yielding the, so called, *line of synchronization* (LOS) [67]. Although the LOS is continuous, it is not a straight diagonal line. This enables the estimation of a *non-parametric rescaling function* between the states of the signal s.

Let $\mathbf{l} \in \mathbb{R}^{N_s}$ denote the LOS. The interpretation of $\mathbf{l}$ is the following: if $l_i = k$, for some $i = 1, \ldots, N_s$, then, the state of the signal s at time i approximates the state at time k. Here, the LOS is a piecewise linear function. Since, in general, $N_s \neq N$, in practice we apply a zero padding to $\mathbf{r}$ in order to obtain a LOS vector $\mathbf{l}$ whose length is equal to that of the index vector $\mathbf{t}$.

Finally, having estimated the LOS, we calculate the first-order differences,

$$d_{l,i} = l_{i+1} - l_i \ , \ i = 2, \ldots, N \ . \tag{3.17}$$

Doing so, the vector $\mathbf{d}_l \in \mathbb{R}^N$ will be of the form,

$$\mathbf{d} = [\texttt{NaN}, \ldots, 0, d_i, 0, 0, \ldots, 0, d_j, 0, \ldots], \tag{3.18}$$

with the zeros corresponding to the intervals where the LOS is constant. Then, given that $d_i \neq 0$ and $d_j \neq 0$, we consider d_i to be the onset time and d_j the offset time of an epoch of significant activity. This interpretation is justified by the fact that the constant segments of the LOS, or equivalently the zero segments of $\mathbf{d}_l$, correspond to time periods in the signal s whose dynamics, as expressed by the corresponding state vectors, are driven by the same seizure.

Chapter 4

Data collection and preprocessing

This chapter provides a short description of the experimental procedure and then describes the method used to obtain the spike trains.

4.1 Experiments

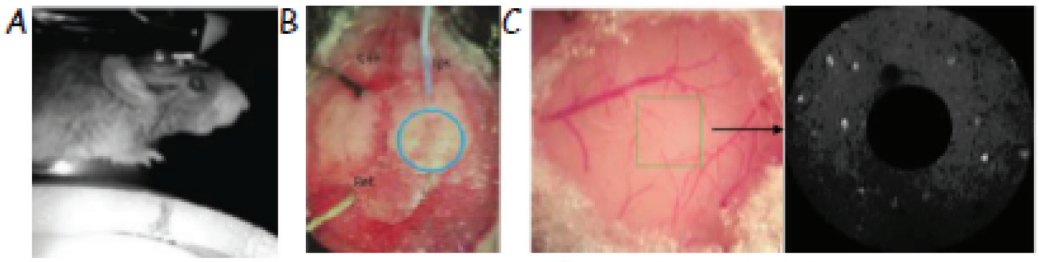

Figure 4.1: A. The mouse is headposted rested awake and free to walk on a treadmill. B. Skull picture showing electrode implantation and site of planned window to overly visual cortex. C. (Left) Craniotomy window after implantation. Green frame illustrates approximately the field of view (FOV). (Right) FOV (diameter $\approx 500\mu m$) showing spontaneous activity prior to the 4-AP injection, scanned by the spiral scanning method. Note that since the spiral is tight at the beginning, the center of the FOV is excluded to avoid causing photodamage.

Animal preparation

All experiments and animal procedures were performed in accordance with guidelines of the National Institutes of Health for the care and use of laboratory animals and were approved by the IACUC at VA Jamaica Plain.

Experiments were performed on an adult (>8 weeks old) Thy1-GCaMP6s mouse which expresses the GCaMP6s calcium indicator in pyramidal neurons [68]. During surgery, mice were anesthetized with 1–2% isoflurane, and Baytril (5 mg/kg), meloxicam (5 mg/kg), and dexamethasone (1.5 mg/kg) were administered subcutaneously to minimize brain swelling [69]. A craniotomy with diameter of 3 mm was made over the center of visual cortex: 2.7 mm lateral to the midline and 1.5 mm anterior to lambda. Then, the craniotomy was covered with a glass window. 1 mm long, flat Ag/AgCl electrodes were placed epidurally over the somatosensory cortex, 2 mm anterior to the midline of the craniotomy, and over the same position on the contralateral hemisphere. A reference electrode was implanted over the cerebellum. Finally, a titanium headpost was permanently attached on the skull with dental cement.

Imaging

Two-photon experiments were performed ∼3 weeks after the surgery, when inflammation had completely subsided. Neurons located ∼150 μm below the pia were imaged with a water-immersion 16×, 0.8 NA (Nikon) objective lenses, in a modified Prairie Ultima IV two-photon laser scanning microscope (Bruker), fed by a Chameleon Ultra II laser (Coherent). Cell populations were imaged at frame rates of ∼5 Hz. The laser power was kept between 20 mW at the surface and 50 mW at depths ¡ 200 μm, at 910 nm wavelength.

We imaged layer 2/3 pyramidal neurons at $\sim$ 150 μm from the pial surface. A 150-200 μl solution of 12.5 μM 4-AP or an equal volume of vehicle (0.9% NaCl) was injected 1 mm antero-laterally to the imaged FoV at the level of the primary visual cortex (V1) at the infragranular layer ($\sim$ 600 μm deep from the pial surface). About 20 min after each injection, the post injection activity was recorded. Each recording lasts approximately 10 min. We have three different measurements for the same mouse: pre-injection (control), then post-vehicle injection, and post-4-AP injection.

Both the animal preparation and the imaging were conducted by Dr. Joseph Lombardo, postdoctoral member of Smirnakis Lab.

4.2 Generation of spike trains - eventograms

The fluorescence recordings obtained through two-photon microscopy were initially preprocessed in order to remove motion correction artifacts and perform regions of interest (ROI) selection in order to end up with the signal that corresponds to each neuron. This stage of the preprocessing was performed by members of Dr. Smirnakis' lab. Next, we refer to this preprocessed signal of the neuron with the term raw fluorescence.

Step 1. Calculate the df/f of each neuron. In order to get rid of the scale of the fluorescence values we are creating the df/f of each neuron, which uses the

baseline of the neuron to create this scale-free version. Over the literature we have seen different definitions of the baseline. We end up to define the baseline as the 10^{th} percentile of the fluorescence signal F. The df/f for each neuron is computed using the following formula:

$$df/f = \frac{F - 10^{th}percentile\ of\ F}{10^{th}percentile\ of\ F} \tag{4.1}$$

Step 2. Run the deconvolution algorithm on df/f. Then we use a deconvolution algorithm in the form that appears in Vogelstein *et al.* [70]. This algorithm is essentially a Bayesian estimation algorithm and yields the most probable spike train given the recorded signal. A linear dependence of the fluorescence on the calcium concentration is assumed. This calcium concentration is taken to decay exponentially to the calcium baseline upon excitation.

Step 3. Calculate noise intervals based on df/f. An issue of this method is that it does not produce binary spike trains, but it rather gives a continuous output s that represents the probability of spike existence at each frame. To convert this into an eventogram a threshold is used. If the deconvolution output is above the threshold an event is inserted, otherwise no event takes place. The way the threshold is set is through the assignment of noise intervals on the df/f. This is done under the assumption that 20 % of the recording contains noise. Under this assumption the $20^{\text{th}}percentile$ corresponds to noise. To find secure noise intervals in the df/f we consider the values where the df/f value is below the $20^{\text{th}}percentile$. To get a more representative noise signal we create an artificial copy of these values over which we assign reflected fluorescence values with respect to the $20^{\text{th}}percentile$. We calculate the $mean + 2standarddeviations$ of this distribution we created and find the frames that have values less than this quantity. All these frames constitute the "noise intervals".

Step 4. Threshold the output of Step 2 to obtain spike trains. Once the "noise intervals" are obtained, we restrict the Vogelstein output signal on these intervals. The threshold used for the Vogelstein output signal is based on the $99^{\text{th}}percentile$ of the noise intervals. The reason for using the $99^{\text{th}}percentile$ of the values of the deconvolved signal found in the noise intervals is that there might be valuable information even in the noise intervals. Moreover, there might be noise even outside the noise intervals and by applying the thresholding we are able to "catch" this noise as well. When the Vogelstein's deconvolution algorithm output is below this threshold we assume no spike (0), otherwise we assume presence of spikes (1). In this way, we end up with spike trains (or eventograms) that let us know about the neuronal firing activity.

A schematic summary of the followed pipeline is presented in Fig. 4.2.

In Appendix A the sensitivity analysis of the used thresholds for the definition of noise intervals and the spike train production is presented. Some examples of

the application of the algorithm on specific neurons of the control and the 4-AP condition are also presented there.

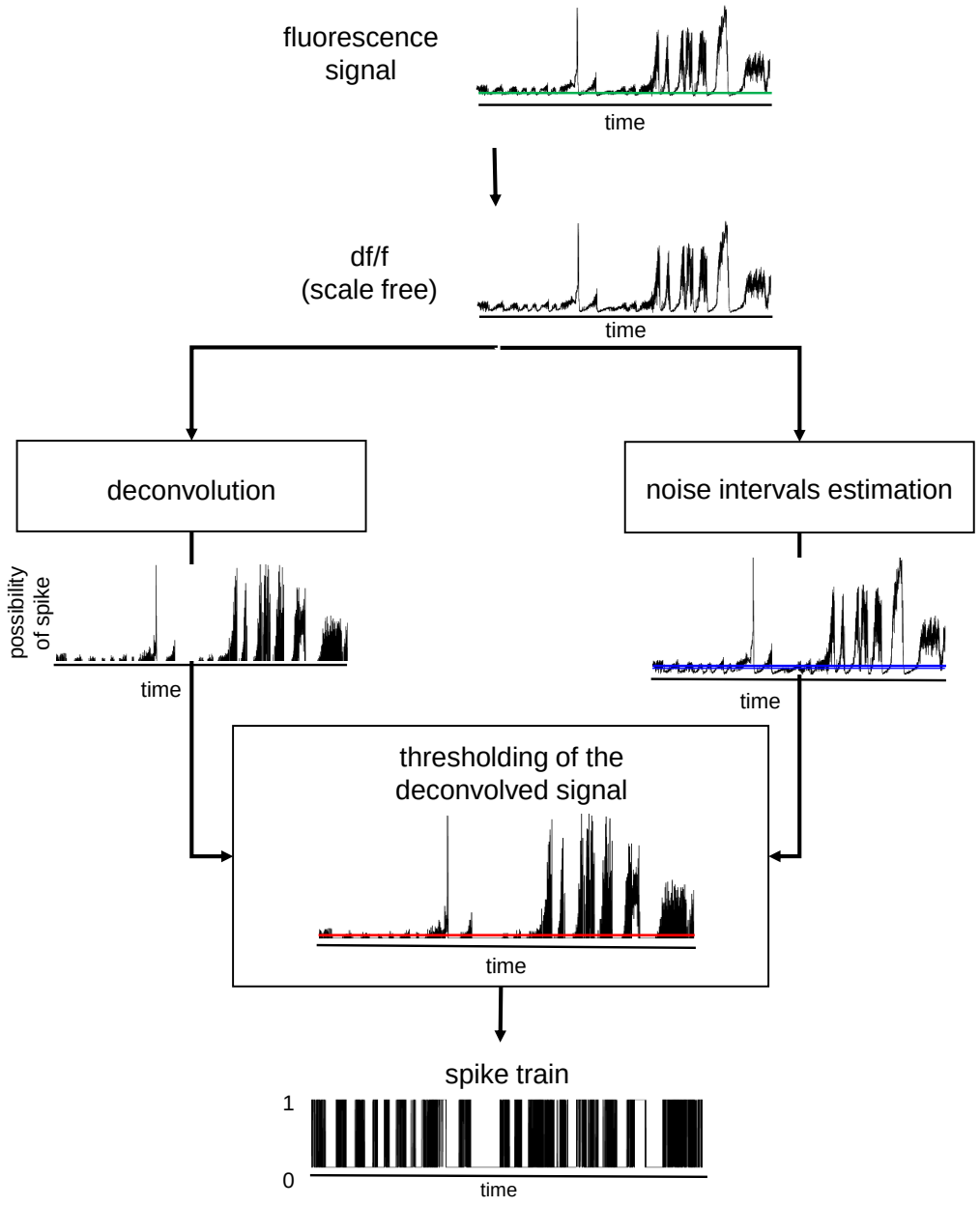

Figure 4.2: Spike train production pipeline. Starting from the fluorescence signal of a neuron, we produce its df/f by subtracting and dividing with the baseline of the signal (10^{th} percentile of the signal). We use the df/f as an iput for the Vogelstein's deconvolution algorithm. This estimates the probability of having a spike at each frame. In order to obtain binary spike trains we need to threshold this probability properly. To this end, we estimate the noise intervals based on the df/f and then project those noise intervals on the deconvolved signal. The frames with values less than the 99^{th} percentile of the noise correspond to 0, while the rest correspond to 1 (spikes).

Chapter 5

Analysis

The results are split into two subsections based on the signals they are based on (spike trains or fluorescence signals). Based on the spike trains and the temporal correlations of the neurons we construct functional connectivity graphs and analyse them in terms of degree of connectivity, clustering coefficient, and affinity. We also compare the acquired graphs with random graphs of known properties. Then, we work on the fluorescence signals of the post 4-AP condition to identify significant activity using two methods: a novel methodology based on the noise intervals of the signal and the recurrent quantification analysis. We study the neuron participation in significant activity epochs and assess the temporal aspect of the recruitment across all significant activity periods. Finally, we analyse the ECoG signals based on the identified periods.

5.1 Functional connectivity analysis

After the 4-AP injection neurons are firing more compared to the control (Fig. 5.1 (left)). Also, population activity is more organized and synchronous, with some periods of complete silence and some periods of high population activity (Fig. 5.1 (right)). From these plots it is also evident that the entire neuronal population gets recruited at specific frames towards the end of the recording.

After producing the spike trains for each condition (control, and after 4-AP injection) as described in Section 4.2, STTC analysis was performed (as described in Section 3.4).

We calculate the temporal correlation of the *synchronous* firing of spike trains of two neurons (i.e., two neurons exhibit a firing event *within the same frame*) as well as the *strictly directional* with lag approximately 0.2 sec (i.e., the firing of two neurons with lag of *exactly* one frame). Note that the strictly directional approach does *not* consider synchronous firing (co-firing within the same frame).

In our data, each FOV was represented as a graph $G(N, E)$, where N is the set of the graph's nodes (neurons) and E the set of the graph's edges, with a square adjacency matrix A whose each element $\alpha_{\mathrm{i,j}}$ was a boolean value, with 1

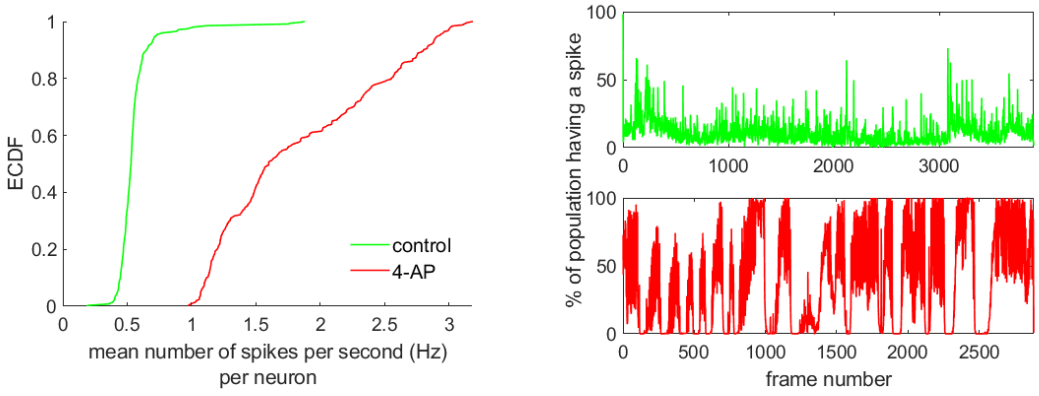

Figure 5.1: Comparative ECDF of mean firing rate of each neuron in control and in post 4-AP condition (left). Percentage of neuronal population having a spike per frame(right).

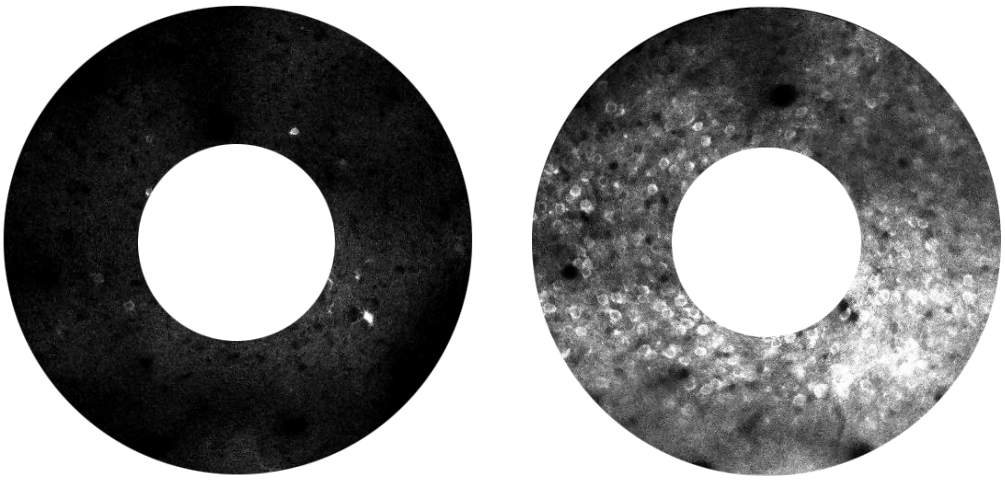

Figure 5.2: Snapshots of the FoV for control (left) and post 4-AP condition (left). Points with lighter color correspond to firing neurons.

if neurons i, j were connected and 0 otherwise. We assigned $\alpha_{\mathrm{i,j}}$ values based on whether the observed STTC value exceeded a $z-score$ threshold. This matrix was symmetrical when graphs were considered to be undirectional, with $\alpha_{\mathrm{i,j}}$ filled with 1 if either $E_{\mathrm{i}\to\mathrm{j}}$ or $E_{\mathrm{j}\to\mathrm{i}}$ existed, i.e. had an STTC value greater than the $z-score$ threshold. For directional graphs, $\alpha_{\mathrm{i,j}}$ were filled with 1 if, and only if, $E_{\mathrm{i}\to\mathrm{j}}$ existed.

Based on the directional STTC with $\Delta t = 0$ (i.e., synchronous case), we define undirectional graphs, while for the case of strictly directional STTC with $\Delta t = 0.2$ sec (1 frame lag) we define directional graphs. For each $z-score$ threshold adopted we compared the degree of connectivity, the percentage of significant edges, and

the clustering coefficient. Please, note that as the $z-score$ threshold gets higher, less and less edges are considered significant.

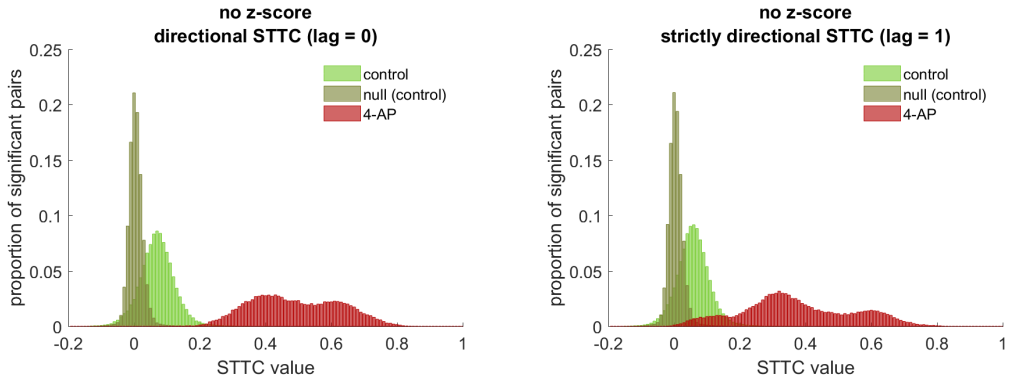

Figure 5.3: STTC values for control and post 4-AP for synchronous STTC (lag 0) (left) and strictly directional STTC (lag 1 frame) (right). All edges included (no $z-score$ threshold applied).

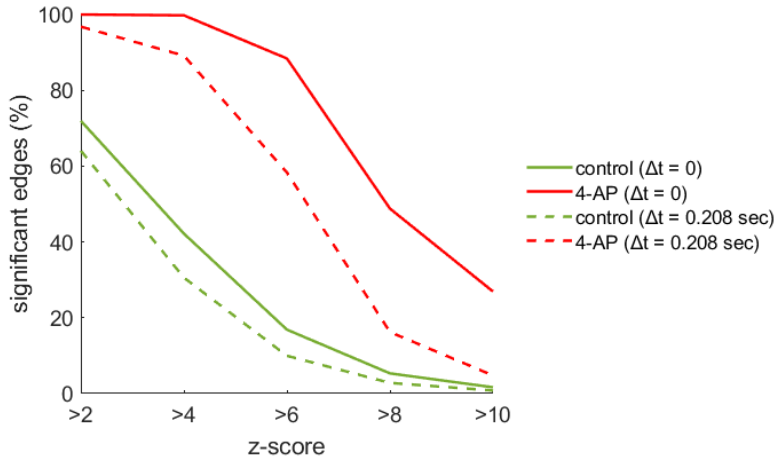

Figure 5.4: Percentage of significant edges for different z-score thresholds both for results of synchronous STTC and results of strictly directional STTC with $\Delta t = 0.208$ sec (1 frame).

Next we characterize the functional network connectivity using graph-theoretical metrics, such as normalized degree of connectivity, clustering coefficient, and weighted clustering coefficient.

Statistically significant temporal correlation in control and post 4-AP conditions. The post 4-AP exhibits significant temporal correlations, stronger than the control, for both the synchronous case as well as the strictly directional with lag of 1 frame (Fig. 5.6, left and right, respectively). The differences of the

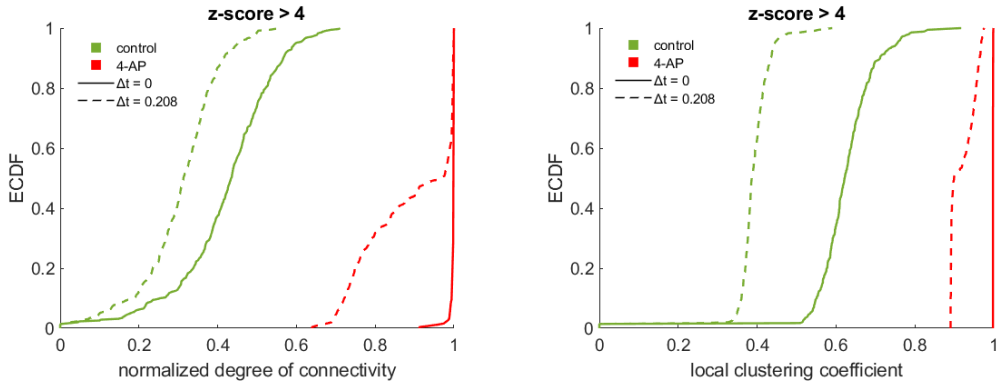

Figure 5.5: ECDFs of (normalized) degree of connectivity (left) and local clustering coefficient (bottom) for $z - score > 4$ (unweighted graphs) for $\Delta t = 0$ and $\Delta t = 0.2$ sec (1 frame) (right).

post 4-AP vs. the control vs. null are prominent.

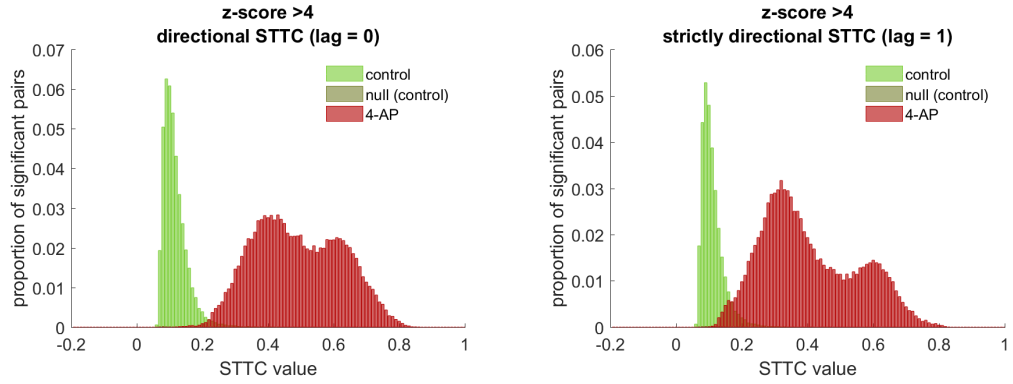

Figure 5.6: STTC values for control and post 4-AP for synchronous STTC (left) and strictly directional STTC (lag of 1 frame) (right). The histograms have been normalized by the total number of possible edges for each case: (only statistically significant edges ($z - score > 4$); the null has a few edges and is not visible.

Dense functional connectivity in post 4-AP condition compared to the control. Compared to the control, post 4-AP exhibits denser functional connectivity, as illustrated with the larger percentage of significant edges, clustering coefficient, and affinity metrics in the synchronous case. The temporal correlation persists in the strictly directional STTC (lag of 1 frame) results.

The strong functional connectivity of the 4-AP condition, higher than that of the control, is illustrated by the high normalized degree of connectivity (normalized as the different FoVs have different number of neurons and we need to make a fair comparison), and weighted directed clustering coefficients as shown in Table 5.2

Table 5.1: Percentage of statistically significant edges

	lag 0	lag 1
4-AP - $z - score > 4$	99.78%	89.14%
control - $z - score > 4$	42.20%	30.57%

Table 5.2: Median normalized degree of connectivity (DoC) & weighted directed clustering coefficient (WCC) for control & post-4-AP (strictly directional STTC with lag of 1 frame); KS test p-value < 0.001.

Graph	DoC	WCC
4-AP	0.996 ± 0.084	0.932 ± 0.037
control	0.580 ± 0.305	0.391 ± 0.120

and Fig. 5.7.

Affinity and Fast Belief Propagation. *The following results are part of the ICASSP 2021 submission, "On Functional Network Connectivity in Focal Neocortical Seizures using Belief-Propagation Metrics" with the valuable contribution of Dr. Maria Markaki using the aforementioned STTC analysis.*

To capture the contribution and influence of a neuron to the connectivity of the network within a larger region, we introduce the *affinity*, a belief-propagation-based metric, that integrates the pairwise temporal correlation of neurons' firing events in a sub-network.

Belief Propagation (BP) combines weak signals to derive stronger ones, employing the principle of the *homophily*. Homophily refers to the tendency of similarly-behavioring nodes to interact with one another in networks. Here we use the Fast Belief Propagation (FaBP), an algorithm that runs two times faster, with equal or higher accuracy than BP, and is guaranteed to converge [57]. It has been extended to weighted, directed networks using weighted non-symmetric adjacency matrices. The incorporation of STTC values in the form of edge weights can produce affinity values which capture more information about the role of the neurons in the network and the diffusion of information.

Prominent differences of the 4-AP compared to the other network topologies. The differences in the topology of the post 4-AP compared to the Erdös-Rényi (ER), Watts-Strogatz (WS), and null graphs are prominent. ER and WS graphs are constructed with the same number of nodes and edges as the 4-AP graph constructed based of strictly directional STTC (lag of 1 frame); their edge

Table 5.3: Affinity for various graphs, equivalent to the post 4-AP (strictly directional STTC with lag of 1 frame, $z - score > 4$); KS test used.

Graph	Median affinity ($\pm$ 2σ)	p-value
4-AP	0.2329 ± 0.0449	-
Null	0.1453 ± 0.0051	< 0.001
ER	0.1766 ± 0.0026	< 0.001
WS	0.1609 ± 0.0009	< 0.001
Control	0.1563 ± 0.0102	< 0.001

weights were all set to the same value, equal to the mean STTC value of 4-AP graph edges. The corresponding statistically significant null graph was constructed as described before (in section 3.4. In the control, a different number of nodes was recorded as we do have slightly different FoVs. Table 5.3 presents the median affinities of nodes of the corresponding graphs. The affinity vector of the 4-AP graph with lag of 1 frame is statistically different from the corresponding control, null, ER, and WS graphs ; p-values for significance of difference of affinities were estimated using the 2-sample K-S test.

Comparing the affinity metric to clustering coefficient. Unlike in the case of 4-AP and control graphs without weights, where their affinity distributions for lag of 1 frame had a small overlap, the weighted affinity distributions of the corresponding graphs, i.e., edges integrated with the STTC weights, are well-separated. Moreover, the weighted affinity reveals an interesting localization property (Fig. 5.7 (top)), which was not present in the case of synchronous graph (Fig. 5.9 (top)). Opposed to clustering coefficient, which is a strictly local metric, the affinity captures the connectivity of a neuron along a larger area (e.g., within a range of 10-hop away neighbors) catching the most active neural network in the 4-AP condition. The lower right part of the FoV is closer the 4-AP injection area, which is the area with the most activity as observed at the video of the recording (Fig. 5.8).

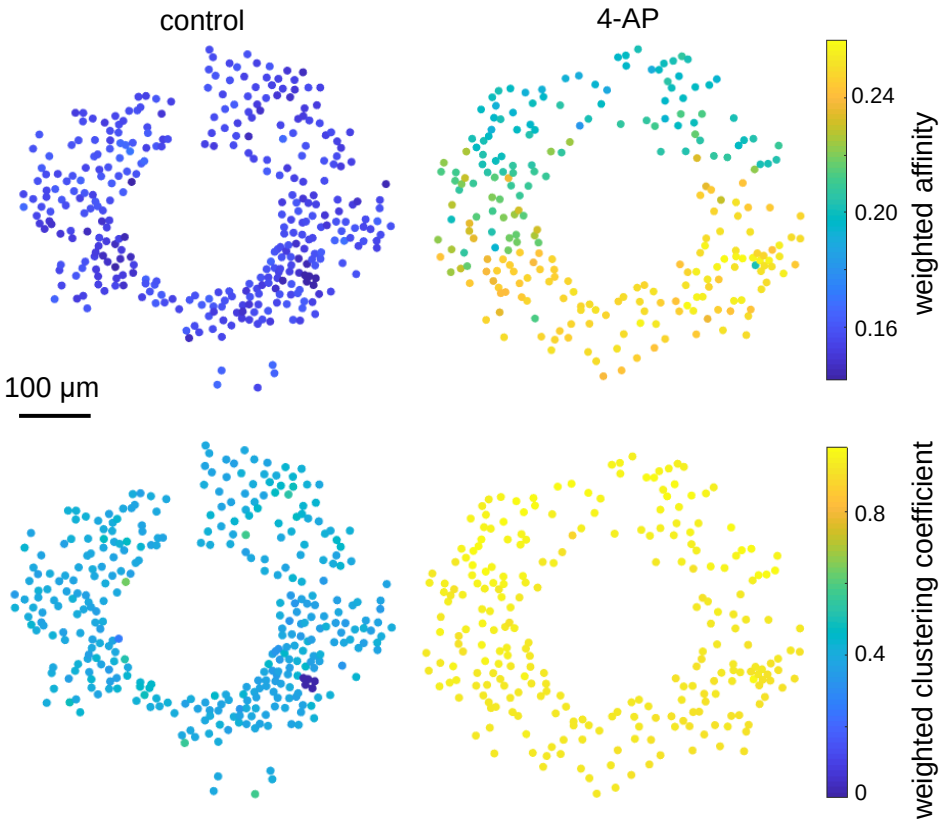

Figure 5.7: Weighted directed affinity (top) compared to weighted directed clustering coefficient (bottom). For the weighted directed graph constructed based on strictly directional STTC (lag of 1 frame) and $z - score > 4$.

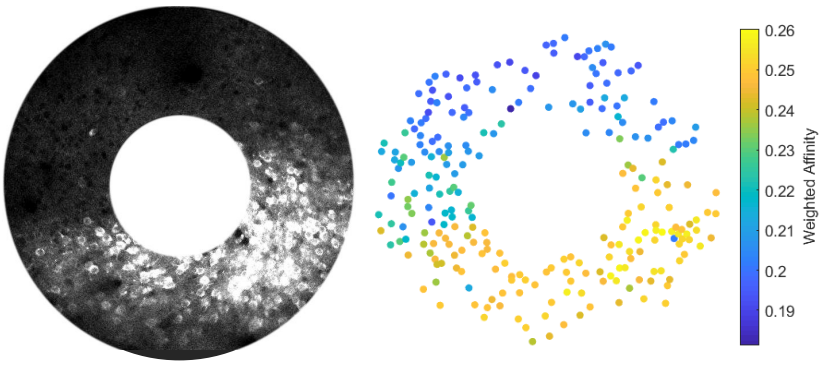

Figure 5.8: Snapshot of the 4-AP recording (left) Weighted directed affinity induces unsupervised clustering of neurons in 4-AP (strictly directional STTC, lag of 1 frame) (right).

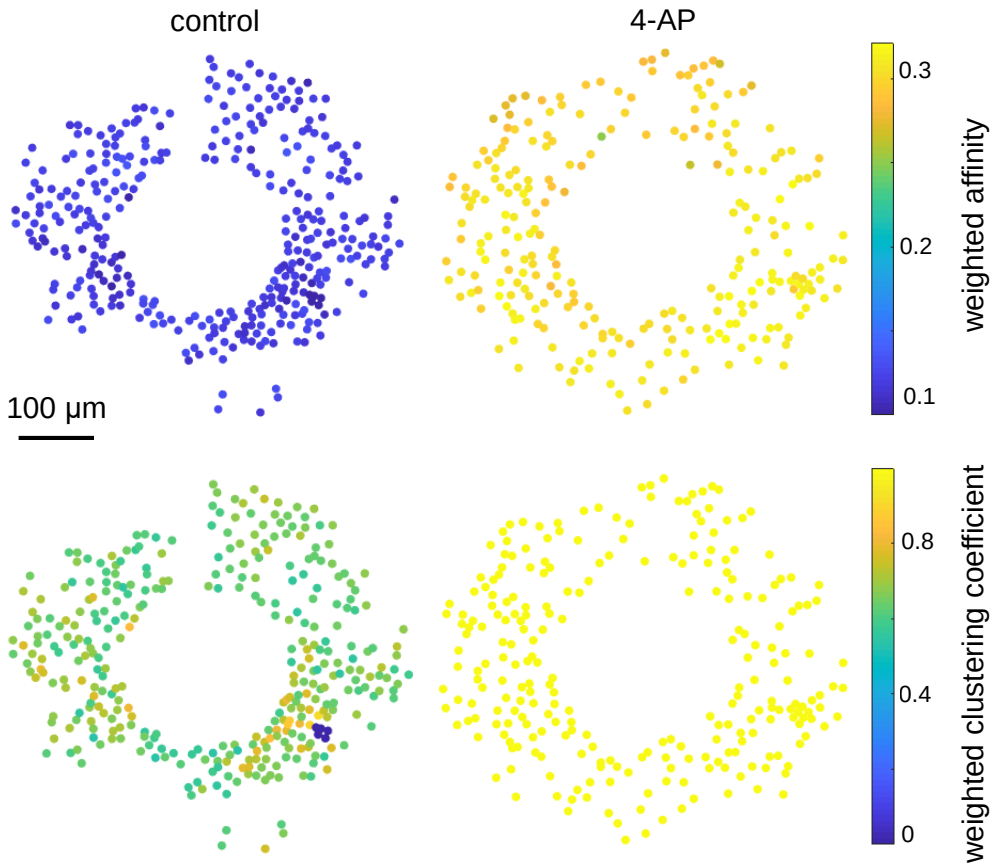

Figure 5.9: Weighted affinity (top) compared to weighted clustering coefficient (bottom). For the weighted undirected graph constructed based on synchronous STTC (lag of 0 frames) and $z - score > 4$.

5.2 Fluorescence-based analysis post 4-AP

Besides the analysis based on the spike trains that provides some insights about the network that is created based on the temporal correlations estimated through the STTC, we work on the fluorescence signals and investigate the existence of significant activity related to seizures and the recruitment of the neurons to them.

5.2.1 Noise-interval-based identification of significant activity epochs

We develop a procedure to identify the epochs of significant fluorescence activity in the post 4-AP recording, called *noise-interval-based* approach.

This procedure first operates on individual neuron level, as follows:
Step A0. Calculate the df/f of each neuron as described in eq. 4.2,

Step A1. Calculate noise intervals for each neuron based on df/f. For that, find the frames with values less than the 20^{th} percentile of the neuron's df/f and "mirror" their values around the 20^{th} percentile we calculated. Then find the frames with df/f less than the 20^{th} percentile + 2 $\times$ standard deviation of this synthetic distribution. These frames are the noise intervals.
Step A2. Count the consecutive frames of the noise intervals. If there are intervals with 7 or less consecutive frames, they are no longer considered as noise interval frames.
Step A3. Count inter-arrival time of remaining noise intervals of previous step. If inter-arrival time is small (7 or less frames), then it will no longer be considered as inter-arrival interval but it will get concatenated together with the prior and following noise interval. Inter-arrivals of larger duration remain the same. **Step A4.** Define as (local) valleys the "cleaned up" noise intervals of the previous step.
Step A5. Define as (local) plateaus the in-between frames. Plateaus correspond to epochs of significant activity.
Step A6. Create a time series for each neuron with 0 at frames of valleys and 1 at plateau frames (this is useful for the global plateau/valley definition as well as the matching of global and local plateaus).

After defining the plateaus and valleys on single neuron level it is time to define them for the entire neuronal population as well. The population or global events are based on the aggregation of the single neuron events:
Step B1. Sum the time series of **Step A6** per frame in order to create the aggregate signal based on which we will define the global valleys and plateaus.
Step B2. Find the frames with 7% or less of the neurons having local plateaus simultaneously in order to define the global level noise intervals.
Step B3. Do **Steps A2-A5** of procedure followed for single neurons to end up with global valleys and plateaus respectively.

Based on the stability of the number of neuron plateaus and the number of global plateaus, we decided to end up with the setting 7 frames for an event to be considered as small and 7% of neurons being active for the definition of the global plateaus and valleys (see Appendix B).

This approach led to the definition of 15 plateaus of varying duration. On individual neuron level the number of plateaus ranges from 14 to 25 (mean 17.6, median 18), also with varying duration. The identified plateaus if to be considered as seizure activity do have differences in terms of duration with the literature reviewed. The median duration of the identified plateaus is 24.5 sec while the mean duration 31.8 sec. However, seizures caused by 4-AP injection reported in recent studies are longer 71± 7.1 sec [53] and 74.4±5.5 seconds [55]. A probable explanation on these differences may be that other studies identified electrographic seizures (based on the LFP measurements), while the plateaus identified in our study are based on the fluorescence of the cells under epileptic conditions.

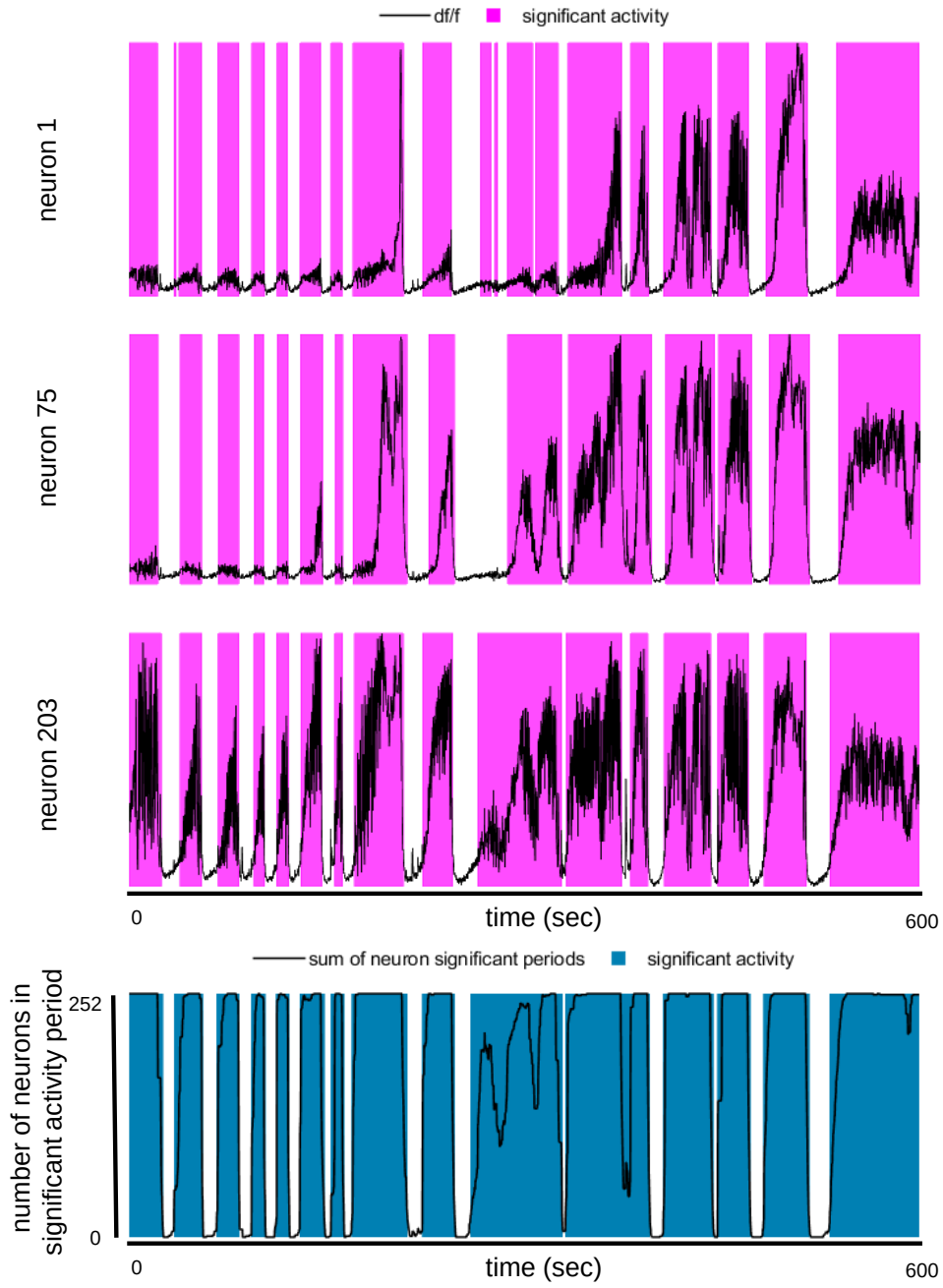

Figure 5.10: Identified significant activity examples. Top 3 panels correspond to examples of significant activity identified 3 different neurons. The bottom one corresponds to the identification of the global significant activity periods based on the identification made on the single neuron level.

5.2.2 Recurrence quantification Analysis.

The following results are part of the ICASSP 2021 submission, "On the Identification and Characterization of epochs of significant changes in Focal Neocortical Seizures" with the contribution of Dr. George Tzagkarakis.

This subsection describes the application of RQA on the population df/f (sum of df/f of all neurons per frame) during epileptic seizures, and comparatively analyses the results with the previous subsection results. We perform the recurrence quantification analysis (RQA) [67, 71] for the detection of critical transitions in the underlying time-evolving dynamics. Specifically, recurrence plots (RPs) were proposed as an advanced graphical technique of visual nonlinear data analysis, which reveals all the times of recurrences, that is, when the phase space trajectory of the dynamical system visits roughly the same area in the phase space. Due to the highly subjective nature of a visual interpretation of RPs, RQA was introduced to perform nonlinear analysis of time series, which is also able to treat non-stationary and short data series. RQA comprises of a set of appropriate quantitative measures for the quantification of recurrence structures, and the detection of critical transitions in the system's dynamics (e.g., deterministic, stochastic), which is precisely one of the two objectives of this work.

Consistent results between RQA and noise-interval based method in the identification of significant activity. The identification of the epochs of significant activity based on the noise-interval approach (plateaus) and the RQA events is shown in Fig. 5.11 (top). After the merging of the small RQA events, according to the same procedure as for the noise-interval-based approach, 16 events remain (marked with green color), while the noise-interval-based identification results in 14 events (marked with blue color). The duration of these events varies (Fig. 5.11 (bottom)). The start and end of events set by the RQA events tend to be earlier and later, respectively, compared with the start and end of the global plateaus identified by the noise-interval-based method. This can be attributed to the time-delayed embedding process, which generates state vectors whose elements may span adjacent regions of the signal with different dynamics. Doing so, RQA is able to "foresee" upcoming switching regimes with respect to the inherent dynamics, when entering these regions ("onset" times), while still maintaining some memory when exiting them ("offset" times).

5.2.3 Recruitment of neurons in plateaus

For each neuron, and for each global plateau, the relative time *lag* of the onset of its local plateau compared to the corresponding global plateau onset is estimated. In order to match the global plateaus with local ones we need to find local events that have at least 1 frame in common with the examined global plateau interval. When more than one local plateaus are matched with a global one, we

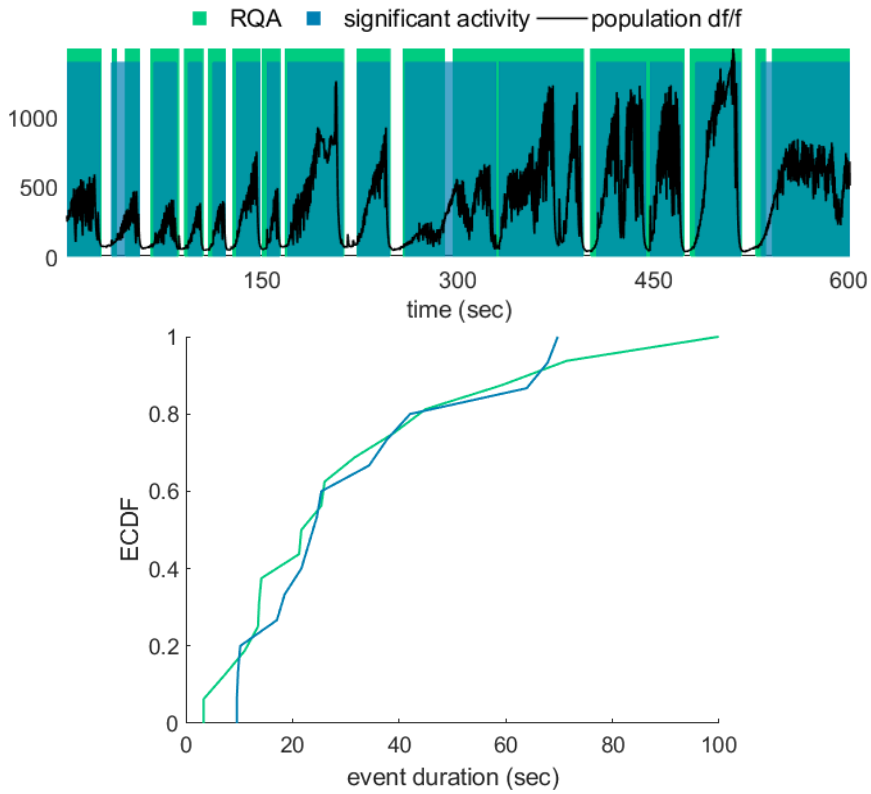

Figure 5.11: Events identified by RQA (green color) and noise interval method (blue color) (top). Comparative ECDFs of the event duration (bottom).

take into consideration only the first one (first in terms of its start). Also, one more convention is followed: in cases that the first local plateau that matches a global plateau has started during the prior global plateau, then this local plateau is not considered for the current global plateau that we are examining. Negative lag means that the neuron's plateau starts prior to the global plateau onset, while positive means the neuron is recruited after the global onset.

Spearman's rank coefficient of plateaus We attempted to assess whether there is a persistent order of recruitment of neurons across all neuron plateaus. To do so, we assigned a number to each neuron id based on the lag it has at each global plateau. The first neuron to be recruited was assigned rank = 1 and the last neuron to be recruited rank = N (number of neurons). If two or more neurons have the same lag for a specific global plateau, this means they should have the same rank, and therefore they are assigned the mean of the ranks they would be assigned if they were ranked individually.

The results of the Spearman's ranking coefficient from the pairwise comparison of the ranks of the global plateaus are presented in Fig. 5.12. There is not very

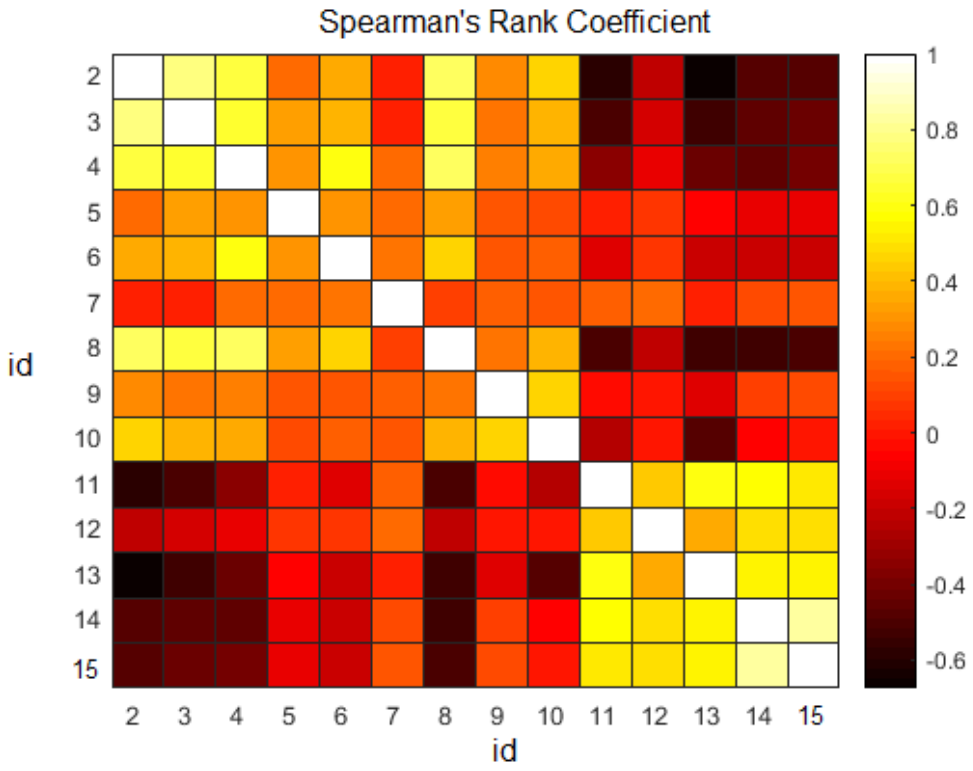

Figure 5.12: Spearman's rank coefficient heatmap. The ids specified on the x-axis and y-axis respectively specify the global plateaus that are compared in a pairwise manner. Note that the 1st global plateau is excluded from this analysis as its start is the start of the recording and we do not have any prior starting neurons.

high rank correlation across all the plateau pairs. Specifically, we see that there are similar high values for consecutive global plateaus at the beginning and towards the end of the recording (the yellow-colored tiles for global plateaus with ids 2-4 and 11-15 in Fig. 5.12). However, in the intermediate plateaus mush smaller values are observed. This is an indication that the order of recruitment is changing as the time passes and the epileptic activity is further propagated in the brain (FoV) farther away from the focal point. Another possible explanation of the small values is that a lot of neurons get recruited (have the onset of their local plateaus) simultaneously, which means they are assigned the same rank with each other. This may in turn affect the results and create big ranking differences which lead in turn to smaller ranking coefficient.

The issues described earlier regarding the Spearman's rank coefficient urged us to use a different approach to evaluate the recruitment order of the neurons. As mentioned earlier, for each global plateau, we estimate the lag of the onset of the corresponding local plateau of each neuron from the onset of that global plateau.

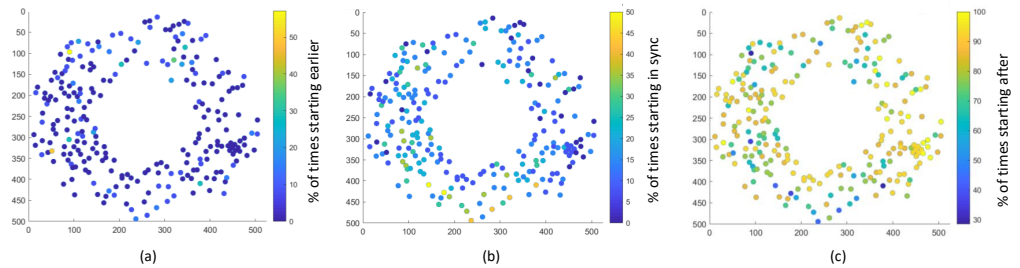

Figure 5.13: Neurons of the post 4-AP FoV colored based on the percentage of global plateaus it starts earlier (a), synchronously (b) or after (c) the global plateau onset.

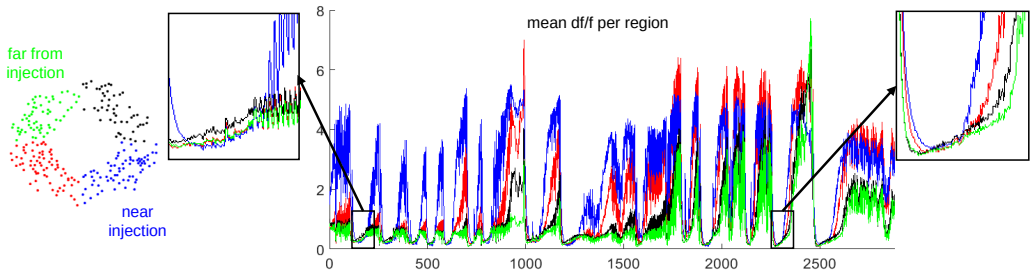

Figure 5.14: Mean df/f of the sub-populations of neurons at the four regions of FoV neurons (colored based on their distances from the injection point). Two representative global plateaus are zoomed to better examine the mean df/f of each region.

We opt to measure for each neuron the percentage of global plateaus at which the matched local plateaus start earlier, are synchronous or are following the global plateaus onsets. This analysis revealed that the majority of neurons get recruited after the onset of the global plateaus. Neurons with onsets before the start of global plateaus are spread all over the FoV (Fig. 5.13), suggesting that the effect of 4-AP is long-range, consistent with observations of Rossi *et al.* [52].

We decided to separate the FoV in 4 regions based on the physical distance from the approximate location of the 4-AP injection (Fig. 5.14, left). This provides a more "mesoscopic" point of view as we are looking the trends per region, and not at single-cell resolution. Taking into consideration the level of the df/f as well as the lags of neurons from different regions, our analysis revealed two phases of the ictogenesis process: In the first phase, up to about the frame 1500 (about first 5min of the recording), the sub-population near the injection point (indicated with the blue color in Fig. 5.14) reaches relatively high df/f levels, while the other three sub-populations have significantly lower values. During that phase, the population closer to the injection has larger lag compared to the other sub-populations, with respect to the global plateaus onsets engagement. As the epileptic activity evolves, the sub-population closer to the injection area starts its ictal-like events earlier than

the others (on average) (Fig. 5.15 (right)) and the df/f gradually increases.

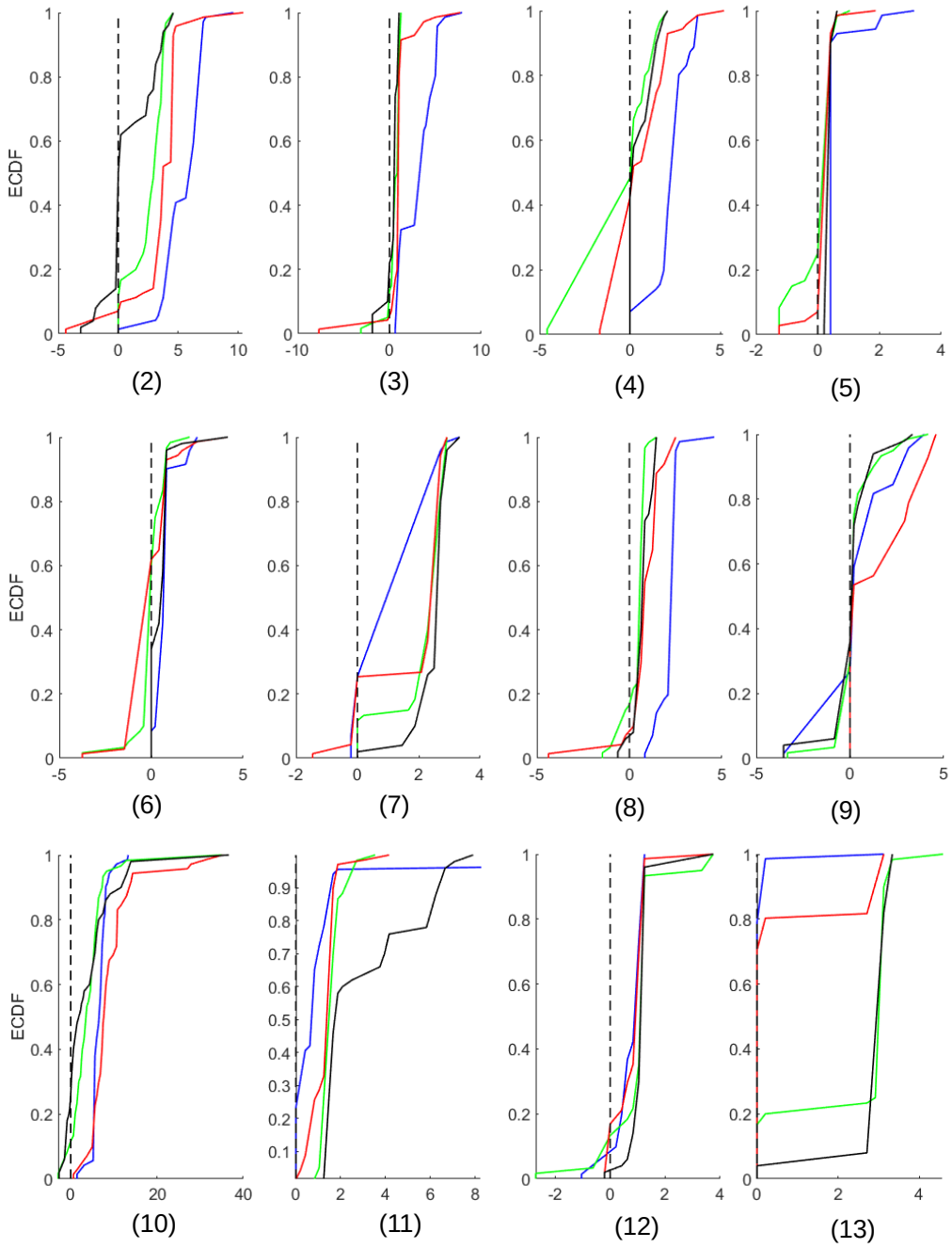

Figure 5.15: ECDFs of the lag of the local plateau of each neuron with respect to the onset of the global plateaus 2 through 13, respectively; colored based on their region as in Fig. 5.14(left).

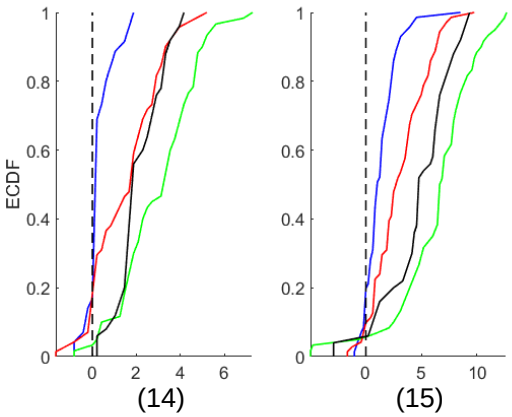

Figure 5.16: ECDFs of the lag of the local plateau of each neuron with respect to the onset of the global plateaus 14 and 15, respectively; colored based on their region as in Fig. 5.14(left).

We do observe that as the epileptic activity evolves there is a gradual increase of the recorded fluorescence level in all 4 regions of the FoV that we defined. This observation is consistent with layer 2/3 pyramidal neurons fluorescence increase in [55].

If we comparatively observe the recruitment lags per region (Fig. 5.15 and 5.16) we do observe some kind of stochastic order. For plateaus 2-6 there are similar trends with the blue population being recruited later on average. For global plateau 7 the sub-population recruitment order changes a lot. However, the trends of plateaus 2-6 are "restored" for the 8^{th}. For the following 4 plateaus the order gradually changes and for 14 and 15 there is similarity with the population near the injection point (blue) leading the activity on average.

5.2.4 Spectral Analysis of ECoG during the identified events

In our experimental setting, besides the two-photon imaging recording, two ECoG electrodes were also used to capture longer range and more aggregate activity. They were placed on the surface of the brain and not in the brain, and tend to pick up the ensemble activity of most of the cortex of the brain hemisphere on which they're placed. One electrode was located antero-laterally to the imaging window (ipsilateral) and another one is located contra-laterally on the other brain hemisphere. The sampling frequency of the ECoG signals was 10kHz.

Before proceeding with the EEG signal analysis some preprocessing took place. First, the 60 Hz frequency component (noise from electric power network) and its harmonics were removed with use of notch filters centered at these specific frequencies. Then, frequencies below 0.5 Hz were also removed with use of high-pass filter and finally a low-pass filter with cut-off frequency of 4000Hz was used to remove the very high frequency components, as higher frequencies do not play

any biological role and are not of interest.

Then, we employed the Welch method (described in Section 3) to study the spectral density of the signals. The window size is set to be small enough to study the short intervals but also big enough to provide sufficient frequency resolution. In case of the analysis of the identified significant activity periods (plateaus) and the noise-intervals the window size was set to 3 sec in order to run for all the available periods. This window size yields frequency resolution of 0.33 Hz.

Energy of the ECoG signal in the 4-AP is higher than that in the control. Specifically, there is a high energy frequency components in the delta band (Fig. 5.17). Interestingly, there are small differences between the dominant frequency components within the delta range, with the contra-lateral side manifesting its highest peak at 1.33 Hz while the ipsi-lateral signal has its own highest peak at 2.66 Hz, indicating that the seizure has affected more the ipsi-lateral part. This may have to do with the fact that the ipsi-lateral hemisphere is more contaminated by the seizure activity and is functioning in a faster way, compared to the contra-lateral hemisphere that is not fully contaminated yet.

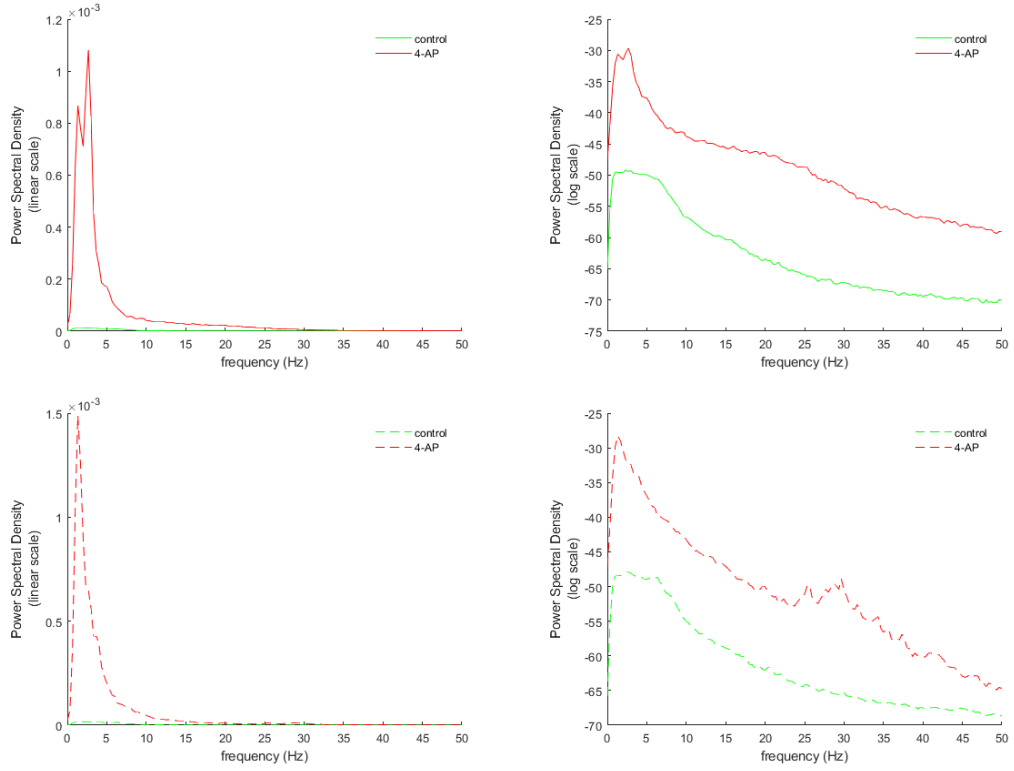

Figure 5.17: Power Spectral Density estimated with the use of Welch method, window size = 3 seconds, 50% overlapping of windows. Linear scale (left) and log scale (right). For the ispilateral (top) and the contralateral (bottom) sides of the brain.

Then we divided the ECoG in post 4-AP condition in intervals equivalent to the plateaus and valleys in order to have indication of their spectral differences. On average during plateaus more energy is released than the during the valleys. However, the standard error of the mean in the acquired plots (Fig. 5.18) shows that there is not a very distinct separation of these events in terms of ECoG energy.

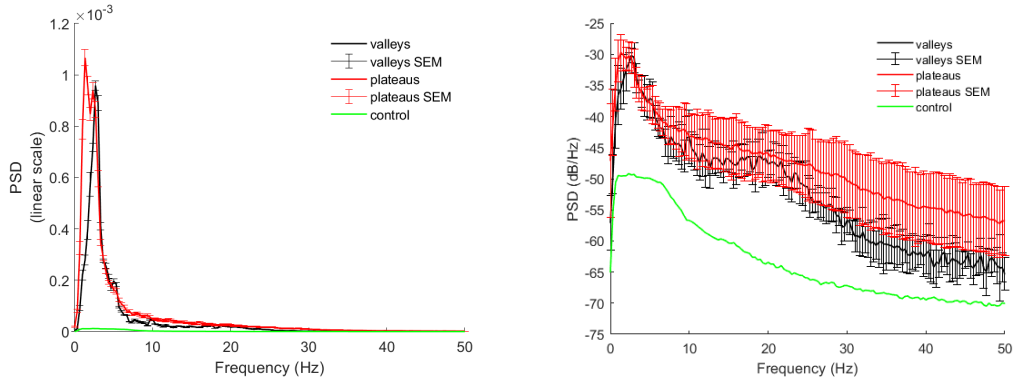

Figure 5.18: Power Spectral Density estimated with the use of Welch method, window size = 3 seconds, 50% overlapping of windows. Linear scale (left) and log scale (right). The error bars indicate the standard error of the mean of the corresponding periods.

Chapter 6

Conclusions and Future Work

This work demonstrates the high temporal correlation of neurons in the context of 4-AP and its denser functional network connectivity, compared to other network architectures and conditions. Moreover, it highlights the power of the weighted graphs and affinity to identify neurons that play an important role in the evolution of the ictogenesis. In contrast to the clustering coefficient and the normalized degree of connectivity metrics, the affinity of the weighted graph helps to identify neurons that are used as proxies of the increased activity after the 4-AP injection. To the best of our knowledge is the first study that discusses the functional network connectivity in the context of 4-AP induced seizures. It has been previously applied in absence epilepsy seizures [72]. Absence epilepsy interrupts normal cortical processing, producing reversible episodes of altered consciousness. During inter-ictal activity, most neurons are functionally connected with a large number of neighbors within the FoV, while in seizure epochs, the connectivity is reduced substantially. The evolution of ictogenesis in 4-AP differs substantially from the absence epilepsy.

The STTC emphasizes on the identified spikes over time to assess the temporal correlation of neuronal activity, while conventional correlation approaches (such as Pearson's correlation) would count coexistence of no spike as correlation, which is not the case. Other 4-AP related studies (e.g., [55]) quantify the temporal correlation of neurons based on their df/f. However, in df/f it is not clear what a spike is and what is not, making the estimation of the temporal correlation a challenging task. The inherent noise in the signal may also introduce "false" correlation to some extent. On the contrary, spike trains are defined with a well-established methodology from the original signals and provide a reliable estimate of the firing events of neurons over time. For this reason a correlation metric (such as Pearson correlation) using df/f will probably not be capable to successfully assess the temporal correlation of firing events.

We also define a methodology to identify the significant activity of the fluorescence signals under epileptic conditions but also used RQA-based techniques

towards that direction. The two approaches yield similar results in terms of number of events and duration. The start and end of events set by the RQA events tend to be earlier and later, respectively, compared with the start and end of the global plateaus identified by the noise-interval-based method. This can be attributed to the time-delayed embedding process, which generates state vectors whose elements may span adjacent regions of the signal with different dynamics. Doing so, RQA is able to "foresee" upcoming switching patterns with respect to the inherent dynamics, when entering these regions ("onset" times), while still maintaining some memory when exiting them ("offset" times). RQA has been previously used to identify seizures in EEG recordings [73, 74, 75, 76], but it the first time that RQA-based techniques are applied to identify the neuronal activity patterns of interest, and dissect, *in vivo*, the mechanisms of focal epilepsy.

We also studied the recruitment of neurons into seizures in differently located regions of the FoV. The Spearman's rank correlation showed different recruitment patterns in the start and the end of the recorded activity. Neurons in general do not play a persistent role to significant activity initiation across the entire recording (starting prior, in sync or starting after). Farther away from the approximate injection point, neuronal activity seems to change the most; At first there are very small amplitude oscillations that gain amplitude as the seizures get expanded in the imaged FoV.

Our long-term objective is to unravel the mechanisms of seizure initiation and propagation to more precisely model *in vivo* epileptic cortical networks. We aim to examine the finer spatio-temporal dynamics of the ictogenesis process, and micro-phases, including the order of the recruitment of neurons in the seizures, integrating information from the EEG. We plan to examine whether the EEG signal may reveal information about the states of other neurons (e.g., interneurons outside the FoV) that may play important role in the propagation or in the control of seizures.

We are in the process of validating the results with other mice recordings. The newly available datasets cover larger periods of time ($\sim$ 1 hour long recordings) and have finer level information (sampling rate: 30 Hz vs. 5 Hz of the currently analysed mouse). In these new datasets, the ROI matching between conditions may be possible and this will enable work on temporal graphs and comparison of these in terms of connectivity and hub creation. So far, we have seen that time plays an important role and as time passes the center of the epileptic activity seem to move further away from the approximate injection area.

We will use the cross correlation of the $df//f$ of neuron pairs within small windows around the global plateau onsets to further study the lags of neurons. Lack of symmetry in the cross correlation of two signals suggests the existence of prominent lags and a leader-follower relationship between these signals. This will help us to better understand the neuronal dynamics and the evolution of seizures in the imaged area. Moreover, we aim to study the slope of the rise and drop of the df/f at the onsets and offsets of the neuronal plateaus and compare/observe the trends of different neurons to perform a profiling of neurons based on the plateaus

dynamics (slope, shape, amplitude, duration of their local plateaus).

In order to indirectly examine the expansion of seizures to farther away regions, such as the motor cortex, the correlation of the plateaus with the speed of the wheel the mouse is moving on will be examined.

We would also like to examine the extent to which the 4-AP injection changes the cortical organisation in general. For that purpose, additional lab measurements were performed on the day after but also some weeks after the 4-AP injection to be able to observe such trends.

The role of the interneuronal activity needs to be examined as well, as it may be particularly revealing about the organization of the brain areas, about the way pyramidal neurons are orchestrated by interneurons, and about how the changes in the balance of inhibitory and excitatory activity affect the epileptic mechanism.

We would also like to model the epilepsy on the graph and predict the next moves of the epileptic spread. More specifically, we would be interested to model the exact behavior of neurons and see what will happen if key neurons or neuronal sub-networks are removed. This way we would be able to design pharmaceutical solutions to stop the expansion of seizures.

To extract the sub-networks with the dominant predictive power on detecting the end of the ictal phases, Long-Short Term Memory (LSTM) networks [77, 78] can be applied. LSTM have been recently applied on EEG data to declare an imminent seizure with an increased accuracy compared to convolutional neural networks and other traditional machine learning approaches [79]. Another study applied a LSTM network on EEG data for the detection of distinctive electrographic events such as epileptic spikes, ripples and ripples-on-spikes [80]. LSTM can nicely integrate the temporal dimension (accurately modeling both short and long-term dependencies in the data) [78] and more specifically the sequence that identified neuronal patterns manifest during the evolution of ictal-events. LSTMs will model the sequence of transitions of these neurons. Specifically, the input layers of LSTM networks will correspond to the actual neurons under different realization conditions, namely spontaneous and focal epileptiform activities. The different types of phases will correspond to the output layer. These LSTM networks will be trained and evaluated using the collected time-series or extracted features, such as, statistical properties of the time-series, power spectral density in specific frequency ranges, graph-theoretical properties based on the significant pairs as reported from the STTC, and RQA analysis. The configuration of the memory "cell" building blocks of these LSTM networks parameters, at the completion of the training and validation of these networks, will reflect the neuronal inter-dependencies (sub-networks) and their impact on predicting the transitions between the various phases of the ictal-like events.

Appendices

Appendix A

Sensitivity analysis of spike train production

Towards the spike train production several decisions should be taken. The first one of them is related to how we are going to define the noise intervals. For that, we performed a sensitivity analysis on the percentile used for the definition of the synthetic distribution of what we do consider as noise.

The initial choice was the use of the 50^{th} percentile. That choice was used based on the assumption that a neuron fires sparsely, i.e. less than 50% of the time. However, this choice seems to be invalid for neurons under epileptic conditions during which we do have neuronal hyper-excitability and increased number of firing events. As the same definition of noise intervals should be used both for the control and epileptic conditions, we opt to lower the percentage of frames considered noisy in order to choose a percentile that manifests small variance of values across all neurons (Fig. A.1). Based on that, the 20^{th} and 30^{th} percentiles of the signal were used as a basis for the noise intervals definitions and the obtained results were comparatively examined.

Another important decision we had to make was related to the threshold applied to the output of the deconvolution algorithm (Vogelstein *et al.* [70]) in order to obtain binary spike trains. Towards that direction we opt to project the calculated noise intervals (based on the df/f) to the deconvolved signal and use a percentile of those projected values as a threshold to decide what is to be considered as a spike and what is not. The reason we project these intervals on the deconvolved signal and then use a percentile of this distribution is to better control the amount of noise allowed but also to take into consideration the noise that can be found outside the noise intervals defined on the df/f. We performed a sensitivity analysis on the applied threshold using the 95^{th} and the 99^{th} percentiles.

The final setting was chosen based on the effect our choices on the neuronal firing rates. The 95^{th} percentile for thresholding of the deconvolved signal results to higher firing rates compared to the case of the 99^{th} percentile. When using the 50^{th} percentile for the noise interval definition we observe that the control and

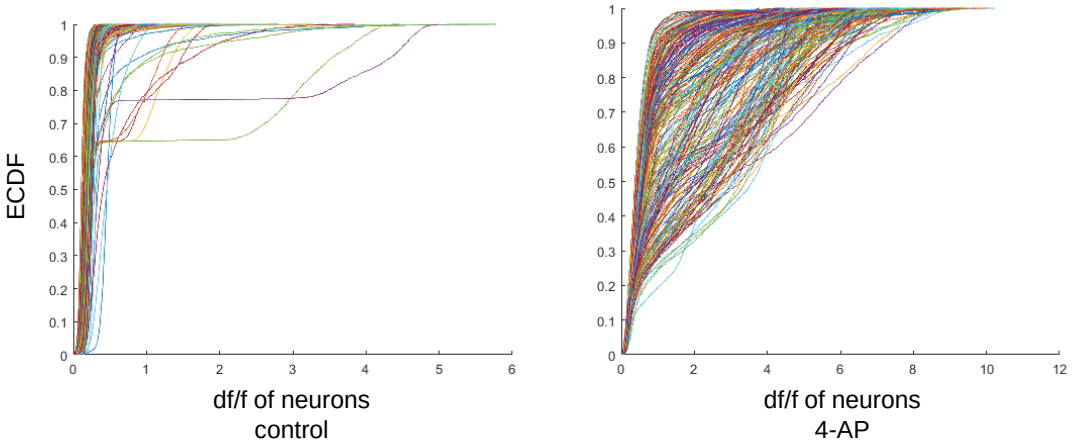

Figure A.1: ECDF of neurons' df/f for control (left) and post 4-AP condition (right). Each plotted line corresponds to one neuron.

4-AP firing rates are having the same range, which is not expected, as in the 4-AP condition we do know that there is more activity. The 30^{th} and the 20^{th} percentiles for the noise interval distribution result in more separable distributions but with the use of 20^{th} percentile we do observe a more clear separation between control and 4-AP conditions (Fig. A.2). In order to come up with the best combination, we compared the resulting firing rates with the ones reported in other studies for awake mice under spontaneous conditions [81, 82].

The aforementioned analysis has been also performed on neuropil subtracted fluorescence signals and we did not observe significant changes (Fig. A.3). Neuropil subtraction is a procedure during which the activity of the surrounding pixels of each ROI (neuron) is subtracted as it is assumed to introduce noise from surrounding neuropil activity and contamination of the fluorescence by the surrounding area.

Some examples of how the procedure looked on individual neurons follow both for control and 4-AP. Such plots were examined one by one for all the neurons (ROIs) in order to find the setting that best captures the neuronal activity without allowing a lot of noisy spikes. For the control the 50^{th} percentile for the noise interval definition works relatively well. However, for the 4-AP conditions in neurons with continuous high activity through the recording this threshold was creating sub-optimal threshold that resulted in reduced firing compared to the actual one.

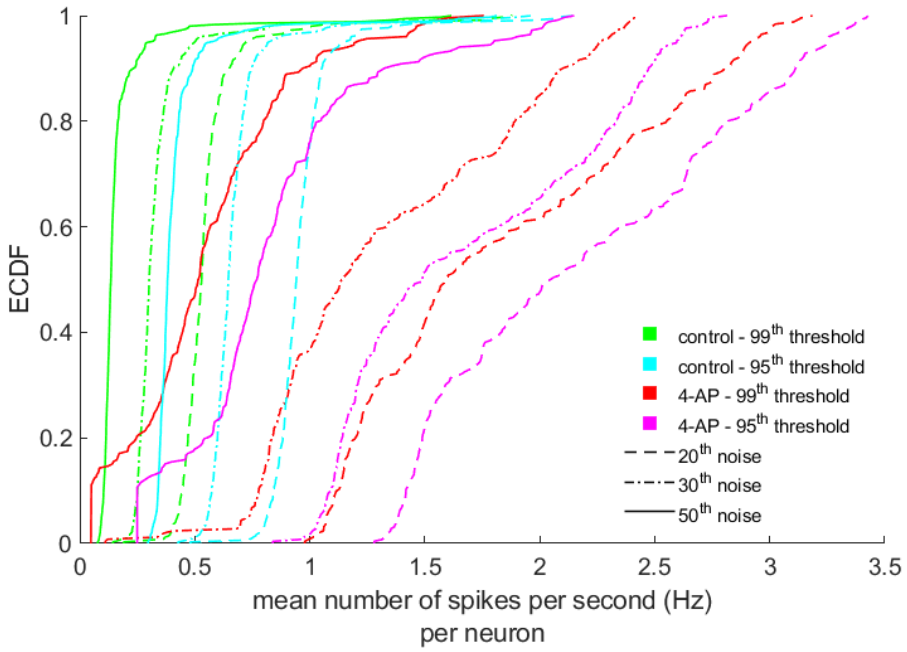

Figure A.2: Comparative ECDFs of neuronal firing rates for different setting combinations of noise interval and deconvolution thresholding.

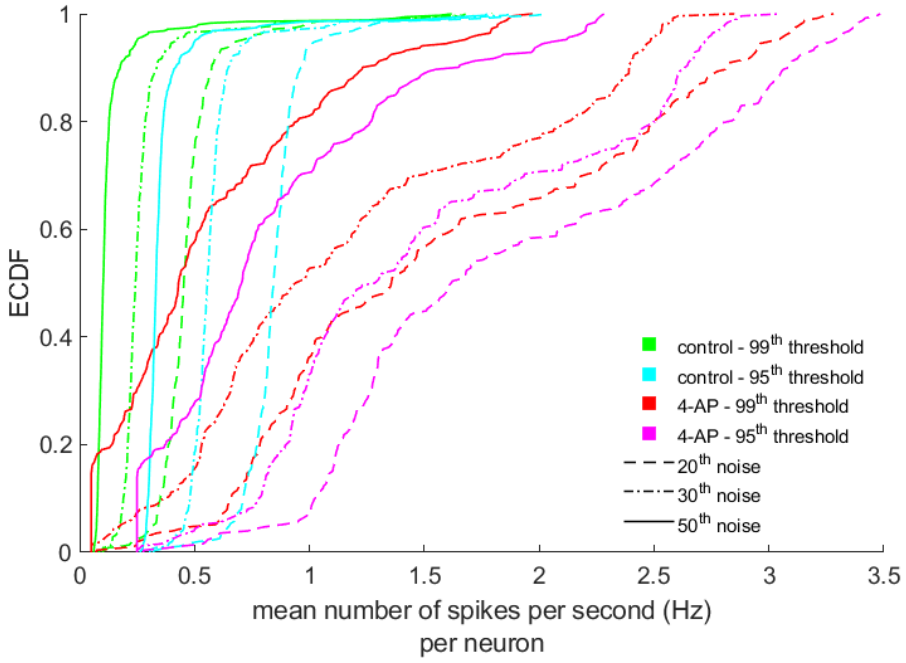

Figure A.3: Comparative ECDFs of neuronal firing rates for different setting combinations of noise interval and deconvolution thresholding for signals after performing neuropil subtraction.

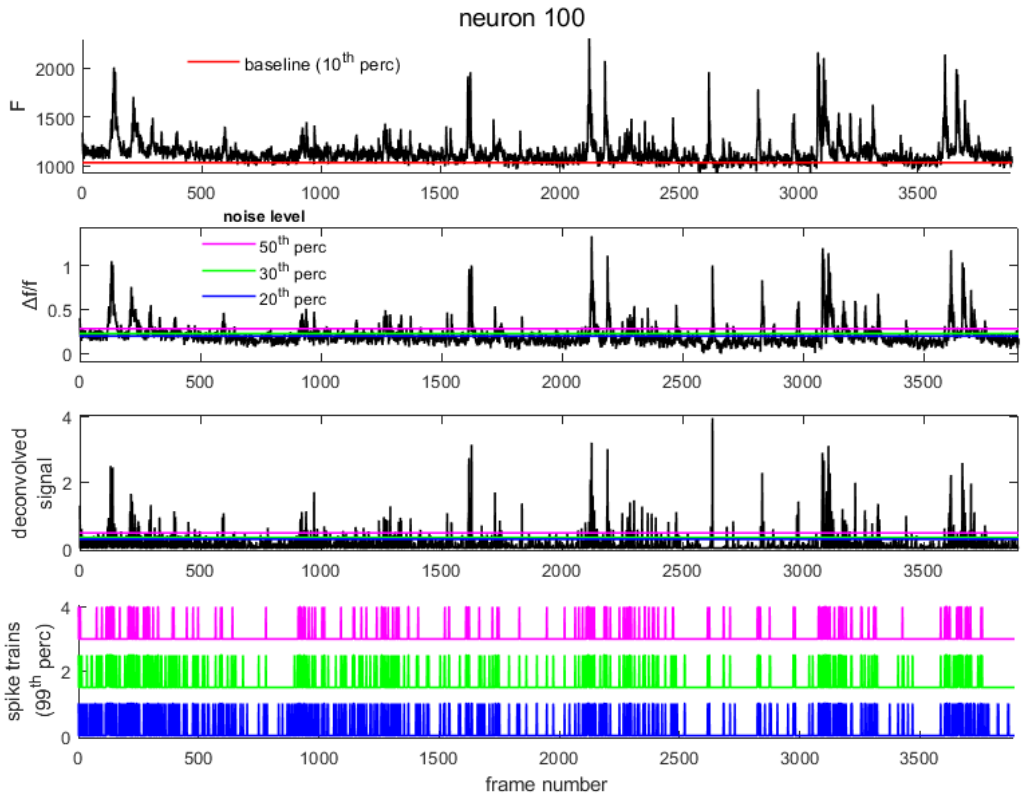

Figure A.4: Steps of spike train production procedure for neuron 100 under normal conditions (control). The 1st vertical panel contains the initial time series and the estimated baseline. The 2nd vertical panel shows the df/f estimated based on the signal and the baseline and the lines that define the noise intervals for different settings examined. The 3rd panel shows the deconvolution result and the thresholds which will result in the spike trains of the 4th panel.

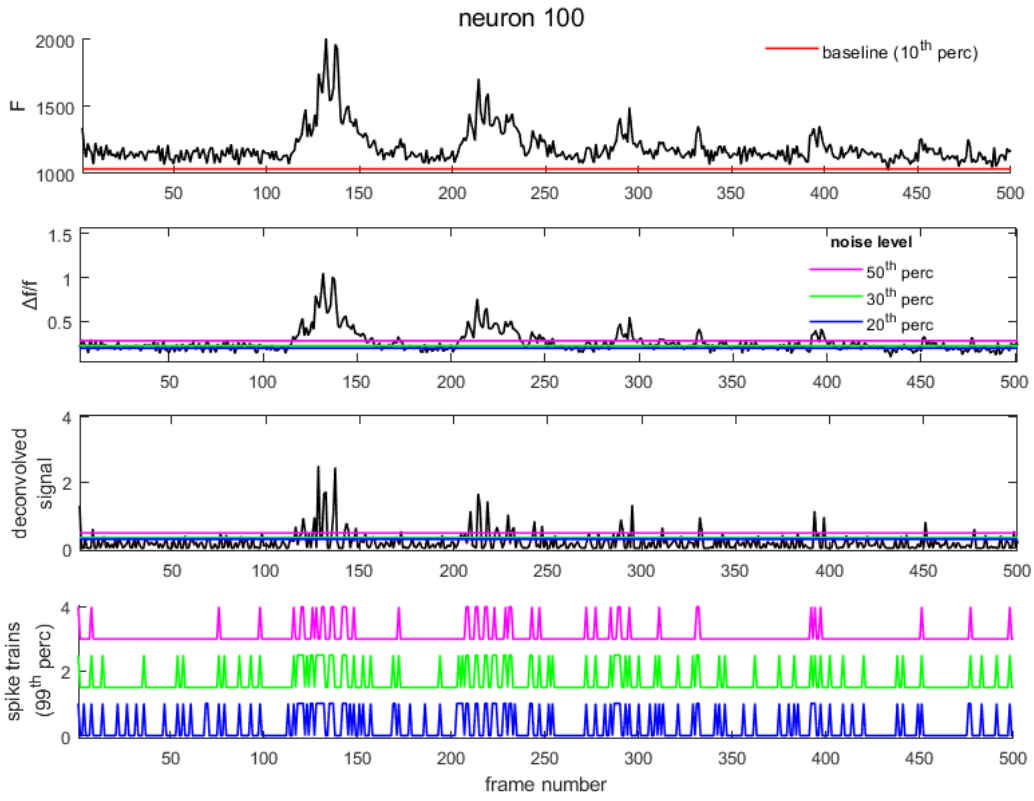

Figure A.5: Steps of spike train production procedure for neuron 100 under normal conditions (control) for a zoomed window of 500 frames ($\sim$ 100 sec) of the signal. The 1$^{\text{st}}$ vertical panel contains the initial time series and the estimated baseline. The 2$^{\text{nd}}$ vertical panel shows the df/f estimated based on the signal and the baseline and the lines that define the noise intervals for different settings examined. The 3$^{\text{rd}}$ panel shows the deconvolution result and the thresholds which will result in the spike trains of the 4$^{\text{th}}$ panel.

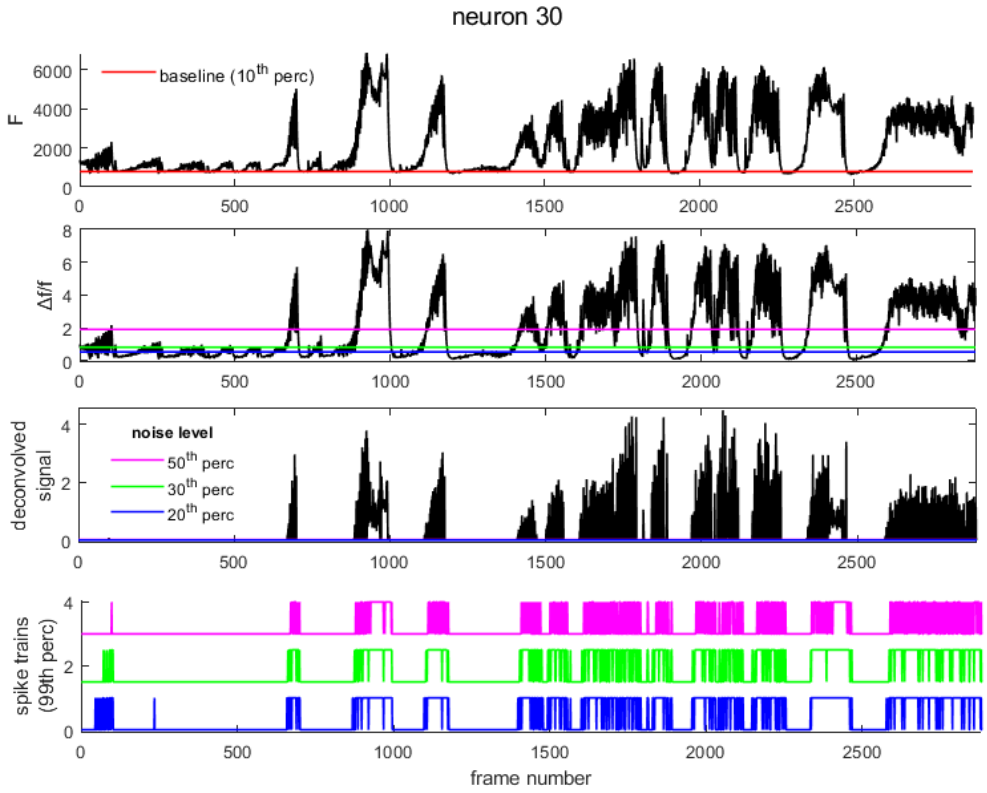

Figure A.6: Steps of spike train production procedure for neuron 30 of post 4-AP condition. The 1st vertical panel contains the initial time series and the estimated baseline. The 2nd vertical panel shows the df/f estimated based on the signal and the baseline and the lines that define the noise intervals for different settings examined. The 3rd panel shows the deconvolution result and the thresholds which will result in the spike trains of the 4th panel.

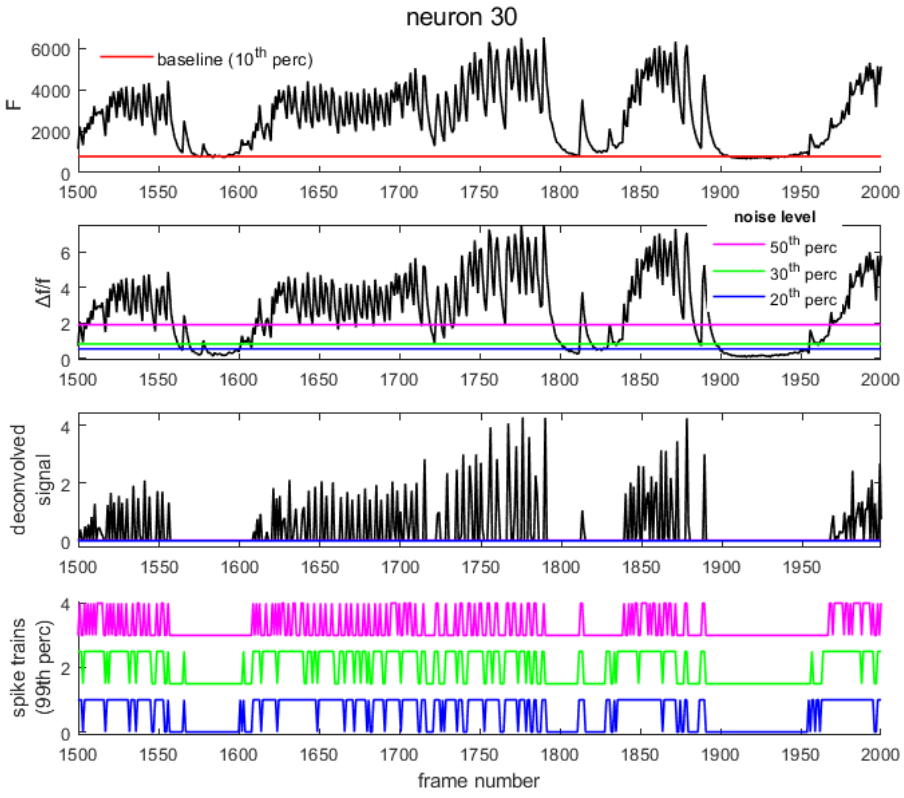

Figure A.7: Steps of spike train production procedure for neuron 30 of post 4-AP condition for a zoomed window of 500 frames ($\sim$ 100 sec) of the signal. The 1^{st} vertical panel contains the initial time series and the estimated baseline. The 2^{nd} vertical panel shows the df/f estimated based on the signal and the baseline and the lines that define the noise intervals for different settings examined. The 3^{rd} panel shows the deconvolution result and the thresholds which will result in the spike trains of the 4^{th} panel.

Appendix B

Sensitivity analysis of identification of significant activity

After making the decision about the noise interval definition (based on what value would the synthetic distribution be centered) we developed the algorithm of the plateaus and valleys analysis.

For the definition of the noise intervals we performed a sensitivity analysis on the number of consecutive frames that we consider as short intervals that need to be treated properly (less than or equal to: 5 to 10 frames). We decided to discard these short intervals noise intervals and perform concatenation of these short inter-arrival intervals with the prior and following noise intervals due to the noisy nature of the df/f signal but also based on the knowledge from prior work that said that seizures should be in the order of several seconds. In our setting, 5 frames = 1 second. One way to alleviate our approach from the need for discarding and/or concatenation of small events could be to use smoothing functions on the signal. However, smoothing tends to displace/move the start and the end of the events earlier and after respectively, which may lead to prolonged events.

We also opt to define the global plateaus based on the individual neurons' plateaus (i.e., taking advantage of the knowledge of the single-cell dynamics). More specifically we decided to use the percentage of neurons having a plateau at the same moment as a criterion for the plateau definition on the entire population. For that reason we performed a sensitivity analysis ranging from 5 to 50% of neurons having a plateau to examine how the number of plateaus change.

Based on the stability of the algorithm (in terms of number of global plateaus and estimated plateau durations) and the need to "catch" the global events early on, we choose the 7% of the neurons to define the onsets and offsets of the global events (Fig. B.1).

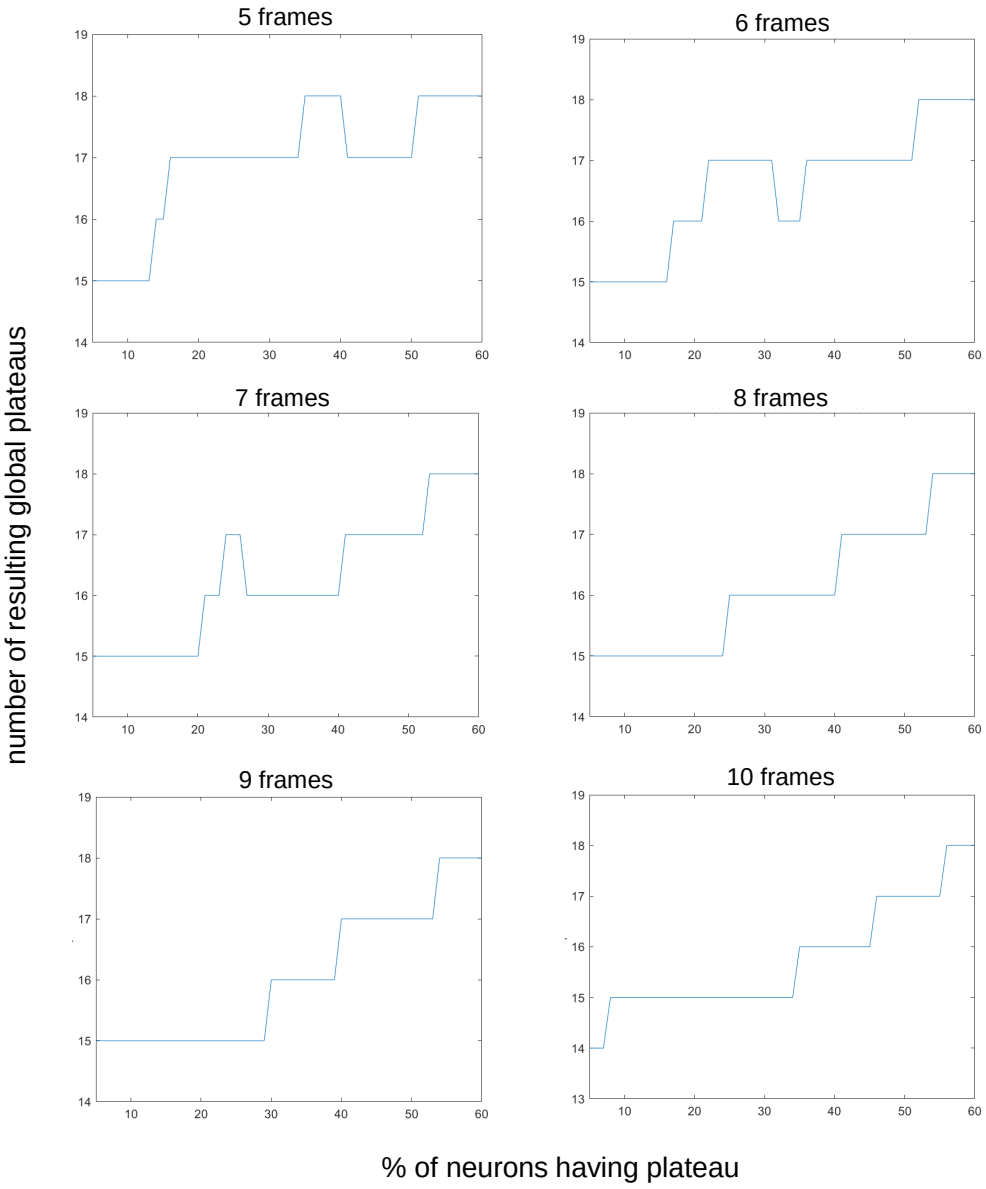

Figure B.1: Results of sensitivity analysis. X-axis corresponds to the number of identified global plateaus based on the % of neurons having their plateau for global plateau onset indicated on the y-axis. The number of frames for considering an interval small is indicated on the top of each plot.

Bibliography

[1] C. S. Cutts and S. J. Eglen, "Detecting pairwise correlations in spike trains: An objective comparison of methods and application to the study of retinal waves," *Journal of Neuroscience*, vol. 34, no. 43, pp. 14288–14303, 2014.

[2] D. McCormick and D. Contreras, "On the cellular and network bases of epileptic seizures," *Annual review of physiology*, vol. 63, p. 815—846, 2001.

[3] V. Raymont, A. Salazar, R. Lipsky, D. Goldman, G. Tasick, and J. Grafman, "Correlates of posttraumatic epilepsy 35 years following combat brain injury," *Neurology*, vol. 75, no. 3, pp. 224–229, 2010.

[4] S. M. Sisodiya and H. C. Mefford, "Genetic contribution to common epilepsies," *Current opinion in neurology*, vol. 24, no. 2, pp. 140–145, 2011.

[5] M. Avoli, M. D'Antuono, J. Louvel, R. Köhling, G. Biagini, R. Pumain, G. D'Arcangelo, and V. Tancredi, "Network and pharmacological mechanisms leading to epileptiform synchronization in the limbic system in vitro," *Progress in neurobiology*, vol. 68(3), pp. 167–207, 2002.

[6] D. Hirtz, D. J. Thurman, K. Gwinn-Hardy, M. Mohamed, A. R. Chaudhuri, and R. Zalutsky, "How common are the "common" neurologic disorders?," *Neurology*, vol. 68, no. 5, pp. 326–337, 2007.

[7] X.-F. Yang and S. M. Rothman, "Focal cooling rapidly terminates experimental neocortical seizures," *Annals of Neurology*, vol. 49, no. 6, pp. 721–726, 2001.

[8] J.-Y. Liou, H. Ma, M. Wenzel, M. Zhao, E. Baird-Daniel, E. H. Smith, A. Daniel, R. Emerson, R. Yuste, T. H. Schwartz, and C. A. Schevon, "Role of inhibitory control in modulating focal seizure spread," *Brain*, vol. 141, pp. 2083–2097, 05 2018.

[9] M. Szente and A. Baranyi, "Mechanism of aminopyridine-induced ictal seizure activity in the cat neocortex," *Brain Research*, vol. 413, no. 2, pp. 368 – 373, 1987.

[10] M. Zhao, H. Ma, M. Suh, and T. H. Schwartz, "Spatiotemporal dynamics of perfusion and oximetry during ictal discharges in the rat neocortex," *Journal of Neuroscience*, vol. 29, no. 9, pp. 2814–2823, 2009.

[11] H. Ma, M. Zhao, and T. H. Schwartz, "Dynamic Neurovascular Coupling and Uncoupling during Ictal Onset, Propagation, and Termination Revealed by Simultaneous In Vivo Optical Imaging of Neural Activity and Local Blood Volume," *Cerebral Cortex*, vol. 23, pp. 885–899, 04 2012.

[12] M. Zhao, L. M. McGarry, H. Ma, S. Harris, J. Berwick, R. Yuste, and T. H. Schwartz, "Optical triggered seizures using a caged 4-Aminopyridine," *Frontiers in Neuroscience*, vol. 9, p. 25, 2015.

[13] M. Zhao, J. Nguyen, H. Ma, N. Nishimura, C. B. Schaffer, and T. H. Schwartz, "Preictal and ictal neurovascular and metabolic coupling surrounding a seizure focus," *Journal of Neuroscience*, vol. 31, no. 37, pp. 13292–13300, 2011.

[14] S. Rothman, "The therapeutic potential of focal cooling for neocortical epilepsy," *Neurotherapeutics : the journal of the American Society for Experimental NeuroTherapeutics*, vol. 6, pp. 251–7, 05 2009.

[15] Z. Gajda, Z. Szupera, G. Blazsó, and M. Szente, "Quinine, a blocker of neuronal cx36 channels, suppresses seizure activity in rat neocortex in vivo," *Epilepsia*, vol. 46, no. 10, pp. 1581–1591, 2005.

[16] R. Hunt, J. Boychuk, and B. Smith, "Neural circuit mechanisms of posttraumatic epilepsy," *Frontiers in Cellular Neuroscience*, vol. 7, p. 89, 2013.

[17] A. Pitkänen, R. J. Immonen, O. H. Gröhn, and I. Kharatishvili, "From traumatic brain injury to posttraumatic epilepsy: What animal models tell us about the process and treatment options," *Epilepsia*, vol. 50, no. s2, pp. 21–29, 2009.

[18] J. T. Paz, C. A. Christian, I. Parada, D. A. Prince, and J. R. Huguenard, "Focal cortical infarcts alter intrinsic excitability and synaptic excitation in the reticular thalamic nucleus," *Journal of Neuroscience*, vol. 30, no. 15, pp. 5465–5479, 2010.

[19] A. Rosen and N. Frumin, "Focal epileptogenesis after intracortical hemoglobin injection," *Experimental Neurology*, vol. 66, no. 2, pp. 277 – 284, 1979.

[20] L. Willmore, G. Sypert, J. Munson, and R. Hurd, "Chronic focal epileptiform discharges induced by injection of iron into rat and cat cortex," *Science*, vol. 200, no. 4349, pp. 1501–1503, 1978.

[21] A. Mihaly, G. Toth, M. Szente, and F. Joó, "Neocortical cytopathology in focal aminopyridine seizures as related to the intracortical diffusion of [^{3}H] 4-Aminopyridine," *Acta Neuropathologica*, vol. 66, pp. 145–154, 2004.

[22] M. Avoli, M. de Curtis, V. Gnatkovsky, J. Gotman, R. Köhling, M. Lévesque, F. Manseau, Z. Shiri, and S. Williams, "Specific imbalance of excitatory/inhibitory signaling establishes seizure onset pattern in temporal lobe epilepsy," *Journal of Neurophysiology*, vol. 115, no. 6, pp. 3229–3237, 2016.

[23] K. Ohki, S. Chung, Y. Ch'ng, P. Kara, and R. C. Reid, "Functional imaging with cellular resolution reveals precise micro-architecture in visual cortex," *Nature*, vol. 433, pp. 597–603, 03 2005.

[24] S. Herculano-Houzel, "The human brain in numbers: a linearly scaled-up primate brain," *Frontiers in Human Neuroscience*, vol. 3, p. 31, 2009.

[25] J. H. Lui, D. V. Hansen, and A. R. Kriegstein, "Development and evolution of the human neocortex," *Cell*, vol. 146, pp. 18 – 36, 2011.

[26] S. Zhou and Y. Yu, "Synaptic E-I balance underlies efficient neural coding," *Frontiers in Neuroscience*, vol. 12, p. 46, 2018.

[27] S. Denéve and C. Machens, "Efficient codes and balanced networks," *Nature Neuroscience*, vol. 19, p. 375–382, 2016.

[28] B. R. Ferguson and W.-J. Gao, "Pv interneurons: Critical regulators of E/I balance for prefrontal cortex-dependent behavior and psychiatric disorders," *Frontiers in Neural Circuits*, vol. 12, p. 37, 2018.

[29] S. Eichler and J. Meier, "E-I balance and human diseases - from molecules to networking," *Frontiers in Molecular Neuroscience*, vol. 1, p. 2, 2008.

[30] E. Kandel, J. Schwartz, and T. Jessell, *Principles of Neural Science*. McGraw-Hill Medical, 2000.

[31] A. T. Berg, S. F. Berkovic, M. J. Brodie, J. Buchhalter, J. H. Cross, W. Van Emde Boas, J. Engel, J. French, T. A. Glauser, G. W. Mathern, S. L. Moshé, D. Nordli, P. Plouin, and I. E. Scheffer, "Revised terminology and concepts for organization of seizures and epilepsies: Report of the ilae commission on classification and terminology, 2005-2009," *Epilepsia*, vol. 51, no. 4, pp. 676–685, 2010.

[32] G. Curia, M. Levitt, J. S. Fender, J. W. Miller, J. Ojemann, and R. D'Ambrosio, "Impact of Injury Location and Severity on Posttraumatic Epilepsy in the Rat: Role of Frontal Neocortex," *Cerebral Cortex*, vol. 21, pp. 1574–1592, 11 2010.

[33] R. D'Ambrosio, C. L. Eastman, F. Darvas, J. S. Fender, D. R. Verley, F. M. Farin, H.-W. Wilkerson, N. R. Temkin, J. W. Miller, J. Ojemann, S. M. Rothman, and M. D. Smyth, "Mild passive focal cooling prevents epileptic seizures after head injury in rats," *Annals of Neurology*, vol. 73, no. 2, pp. 199–209, 2013.

[34] S. Feldt, P. Bonifazi, and R. Cossart, "Dissecting functional connectivity of neuronal microcircuits: experimental and theoretical insights," *Trends in Neurosciences*, vol. 34, no. 5, pp. 225 – 236, 2011.

[35] M. Steriade, *The Intact And Sliced Brain*. Cambridge, Massachusetts: MIT Press, 2000.

[36] W. Denk, J. Strickler, and W. Webb, "Two-photon laser scanning fluorescence microscopy," *Science*, vol. 248, no. 4951, pp. 73–76, 1990.

[37] T.-W. Chen, T. J. Wardill, Y. Sun, S. R. Pulver, S. L. Renninger, A. Baohan, E. R. Schreiter, R. A. Kerr, M. B. Orger, V. Jayaraman, L. L. Looger, K. Svoboda, and D. S. Kim, "Ultrasensitive fluorescent proteins for imaging neuronal activity," *Nature*, vol. 499, pp. 295–300, 2013.

[38] S. M. Potter, "Vital imaging: Two photons are better than one," *Current Biology*, vol. 6, no. 12, pp. 1595 – 1598, 1996.

[39] S. Moffett, S. O'Malley, S. Man, D. Hong, and J. Martin, "Dynamics of high frequency brain activity," *Scientific Reports*, vol. 7, 12 2017.

[40] D. Pizarro, A. Ilyas, G. Chaitanya, E. Toth, A. Irannejad, A. Romeo, K. O. Riley, L. Iasemidis, and S. Pati, "Spectral organization of focal seizures within the thalamotemporal network," *Annals of Clinical and Translational Neurology*, vol. 6, no. 9, pp. 1836–1848, 2019.

[41] W. Jing, Y. Wang, G. Fang, M. Chen, M. Xue, D. Guo, D. Yao, and Y. Xia, "EEG bands of wakeful rest, slow-wave and rapid-eye-movement sleep at different brain areas in rats," *Frontiers in Computational Neuroscience*, vol. 10, p. 79, 2016.

[42] A. J. Watrous, D. J. Lee, A. Izadi, G. G. Gurkoff, K. Shahlaie, and A. D. Ekstrom, "A comparative study of human and rat hippocampal low-frequency oscillations during spatial navigation," *Hippocampus*, vol. 23, no. 8, pp. 656–661, 2013.

[43] A. Maheshwari and J. L. Noebels, "Chapter 12 - monogenic models of absence epilepsy: windows into the complex balance between inhibition and excitation in thalamocortical microcircuits," in *Genetics of Epilepsy*, vol. 213 of *Progress in Brain Research*, pp. 223 – 252, Elsevier, 2014.

[44] M. Lévesque and M. Avoli, "High-frequency oscillations and focal seizures in epileptic rodents," *Neurobiology of Disease*, vol. 124, pp. 396 – 407, 2019.

[45] S. Sanei and J. A. Chambers, *EEG Signal Processing*. New York: Wiley, 2007.

[46] S. Kellis, L. Sorensen, F. Darvas, C. Sayres, K. O'Neill, R. B. Brown, P. House, J. Ojemann, and B. Greger, "Multi-scale analysis of neural activity in humans:

Implications for micro-scale electrocorticography," *Clinical Neurophysiology*, vol. 127, no. 1, pp. 591 – 601, 2016.

[47] G. Schalk and E. C. Leuthardt, "Brain-computer interfaces using electrocorticographic signals," *IEEE Reviews in Biomedical Engineering*, vol. 4, pp. 140–154, 2011.

[48] S. W. Hughes and V. Crunelli, "Thalamic mechanisms of EEG alpha rhythms and their pathological implications," *The Neuroscientist*, vol. 11, no. 4, pp. 357–372, 2005.

[49] M. Avoli, M. Barbarosie, A. Lücke, T. Nagao, V. Lopantsev, and R. Köhling, "Synchronous gaba-mediated potentials and epileptiform discharges in the rat limbic system in vitro," *Journal of Neuroscience*, vol. 16, no. 12, pp. 3912–3924, 1996.

[50] J. Klueva, T. Munsch, D. Albrecht, and H.-C. Pape, "Synaptic and non-synaptic mechanisms of amygdala recruitment into temporolimbic epileptiform activities," *European Journal of Neuroscience*, vol. 18, no. 10, pp. 2779–2791, 2003.

[51] C. Brückner and U. Heinemann, "Effects of standard anticonvulsant drugs on different patterns of epileptiform discharges induced by 4-Aminopyridine in combined entorhinal cortex-hippocampal slices," *Brain Research*, vol. 859, no. 1, pp. 15 – 20, 2000.

[52] L. F. Rossi, R. C. Wykes, D. M. Kullmann, and M. Carandini, "Focal cortical seizures start as standing waves and propagate respecting homotopic connectivity," *Nature Communications*, vol. 8, 2017.

[53] M. Wenzel, J. P. Hamm, D. S. Peterka, and R. Yuste, "Reliable and elastic propagation of cortical seizures in-vivo," *Cell Reports*, vol. 19, no. 13, pp. 2681–2693, 2017.

[54] M. Wenzel, J. P. Hamm, D. S. Peterka, and R. Yuste, "Acute focal seizures start as local synchronizations of neuronal ensembles," *Journal of Neuroscience*, vol. 39, no. 43, pp. 8562–8575, 2019.

[55] F. Aeed, T. Shnitzer, R. Talmon, and Y. Schiller, "Layer- and cell-specific recruitment dynamics during epileptic seizures in vivo," *Annals of Neurology*, vol. 87, no. 1, pp. 97–115, 2020.

[56] A. Gibbons, *Algorithmic Graph Theory*. Cambridge: Cambridge University Press, 1985.

[57] D. Koutra, T.-Y. Ke, U. Kang, D. H. P. Chau, H.-K. K. Pao, and C. Faloutsos, "Unifying guilt-by-association approaches: Theorems and fast algorithms," in *Machine Learning and Knowledge Discovery in Databases*, pp. 245–260, Springer Berlin Heidelberg, 2011.

[58] P. Erdős and A. Rényi, "On the evolution of random graphs," in *Publicatin of the Mathematical Institute of the Hungarian Academy of Sciences*, pp. 17–61, 1960.

[59] D. Watts and S. Strogatz, "Collective dynamics of "small-world" networks," *Nature*, vol. 393, p. 440–442, 1998.

[60] H. Mehlhorn and F. Schreiber, *Small-World Property*, pp. 1957–1959. New York, NY: Springer New York, 2013.

[61] P. Stoica and R. L. Moses, *Spectral Analysis of Signals*. Pearson, 2005.

[62] M. Bartlett, "Smoothing periodograms from time-series with continuous spectra," *Nature*, vol. 161, p. 686–687, 1948.

[63] P. Welch, "The use of fast fourier transform for the estimation of power spectra: A method based on time averaging over short, modified periodograms," *IEEE Transactions on Audio and Electroacoustics*, vol. 15, no. 2, pp. 70–73, 1967.

[64] S. Dowdy, S. Wearden, and D. Chilko, *Statistics for Research, 3rd Edition*. New York: Wiley, 2004.

[65] A. M. Fraser and H. L. Swinney, "Independent coordinates for strange attractors from mutual information," *Phys. Rev. A*, vol. 33, pp. 1134–1140, Feb. 1986.

[66] M. B. Kennel, R. Brown, and H. D. Abarbanel, "Determining embedding dimension for phase-space reconstruction using a geometrical construction," *Phys. Rev. A*, vol. 45, p. 3403, 1992.

[67] N. Marwan, M. Thiel, and N. R. Nowaczyk, "Cross recurrence plot based synchronization of time series," *Nonlinear Processes in Geophysics*, vol. 9, no. 3, pp. 325–331, 2002.

[68] H. Dana, T.-W. Chen, A. Hu, B. C. Shields, C. Guo, L. L. Looger, D. S. Kim, and K. Svoboda, "Thy1-GCaMP6 transgenic mice for neuronal population imaging in vivo," *PLOS ONE*, vol. 9, pp. 1–9, 09 2014.

[69] A. Holtmaat, T. Bonhoeffer, D. K. Chow, J. Chuckowree, V. De Paola, S. B. Hofer, M. Hübener, T. Keck, G. Knott, W.-C. A. Lee, R. Mostany, T. D. Mrsic-Flogel, E. Nedivi, C. Portera-Cailliau, K. Svoboda, J. T. Trachtenberg, and L. Wilbrecht, "Long-term, high-resolution imaging in the mouse neocortex through a chronic cranial window," *Nature Protocols*, vol. 4, p. 1128–1144, 2009.

[70] J. T. Vogelstein, A. M. Packer, T. A. Machado, T. Sippy, B. Babadi, R. Yuste, and L. Paninski, "Fast nonnegative deconvolution for spike train inference

from population calcium imaging," *Journal of Neurophysiology*, vol. 104, no. 6, pp. 3691–3704, 2010.

[71] N. Marwan, M. C. Romano, M. Thiel, and J. Kurths, "Recurrence plots for the analysis of complex systems," *Physics Reports*, vol. 438, pp. 237–329, 2007.

[72] M. Kampourakis, A. Zacharakis, O. Mousouros, G. Palagina, J. Meyer, S. M. Smirnakis, I. Smyrnakis, and M. Papadopouli, "Functional network connectivity analysis in absence epilepsy using stargazer mice," in *2019 IEEE 19th International Conference on Bioinformatics and Bioengineering (BIBE)*, pp. 783–790, 2019.

[73] U. R.Acharya, S. Vinitha Sree, G. Swapna, R. J. Martis, and J. S. Suri, "Automated EEG analysis of epilepsy: A review," *Knowledge-Based Systems*, vol. 45, pp. 147 – 165, 2013.

[74] U. R. Acharya, S. V. Sree, S. Chattopadhyay, W. Yu, and P. C. Ang, "Application of recurrence quantification analysis for the automated identification of epileptic EEG signals," *International Journal of Neural Systems*, vol. 21, no. 03, pp. 199–211, 2011. PMID: 21656923.

[75] E. J. Ngamga, S. Bialonski, N. Marwan, O. Kurths, C. Geier, and K. Lehnertz, "Evaluation of selected recurrence measures in discriminating pre-ictal and inter-ictal periods from epileptic EEG data," *Physics Letters A*, vol. 380, no. 16, pp. 1419 – 1425, 2016.

[76] I. Gruszczyńska, R. Mosdorf, P. Sobaniec, M. Zochowska-Sobaniec, and M. Borowska, "Epilepsy identification based on EEG signal using RQA method," *Advances in Medical Sciences*, vol. 64, no. 1, pp. 58 – 64, 2019.

[77] F. A. Gers, "Long short-term memory in recurrent neural networks," 2001. Ph.D. Thesis.

[78] F. A. Gers, N. N. Schraudolph, and J. Schmidhuber, "Learning precise timing with lstm recurrent networks," *Journal of Machine Learning Research*, vol. 3, no. null, p. 115–143, 2003.

[79] K. M. Tsiouris, V. C. Pezoulas, M. Zervakis, S. Konitsiotis, D. D. Koutsouris, and D. I. Fotiadis, "A long short-term memory deep learning network for the prediction of epileptic seizures using EEG signals," *Computers in Biology and Medicine*, vol. 99, pp. 24 – 37, 2018.

[80] A. V. Medvedev, G. I. Agoureeva, and A. M. Murro, "A long short-term memory neural network for the detection of epileptiform spikes and high frequency oscillations," *Scientific Reports*, vol. 9, 2019.

[81] Q. Perrenoud, C. M. A. Pennartz, and L. J. Gentet, "Membrane potential dynamics of spontaneous and visually evoked gamma activity in v1 of awake mice," *PLOS Biology*, vol. 14, pp. 1–21, 02 2016.

[82] Y. Senzai, A. Fernandez-Ruiz, and G. Buzsáki, "Layer-specific physiological features and interlaminar interactions in the primary visual cortex of the mouse," *Neuron*, vol. 101, no. 3, pp. 500 – 513.e5, 2019.